2014-05-01

# Analysis and Realization of a Dual-Nacelle Tiltrotor Aerial Vehicle

Paul Heslinga
*Worcester Polytechnic Institute*

# Analysis and Realization of a Dual-Nacelle Tiltrotor Aerial Vehicle

by

Paul Heslinga

A Thesis

Submitted to the Faculty

of the

WORCESTER POLYTECHNIC INSTITUTE

In partial fulfillment of the requirements for the

Degree of Master of Science

in

Robotics Engineering

by

Paul Heslinga

May 2014

APPROVED:

Professor Stephen S. Nestinger, Thesis Advisor

Professor Gregory S. Fischer, Graduate Committee Member

Professor Cagdas Onal, Graduate Committee Member

## Abstract

Unmanned aerial vehicles are a salient solution for rapid deployment in disaster relief, search and rescue, and warfare operations. In these scenarios, the agility, maneuverability and speed of the UAV are vital components towards saving human lives, successfully completing a mission, or stopping dangerous threats. Hence, a high speed, highly agile, and small footprint unmanned aerial vehicle capable of carrying minimal payloads would be the best suited design for completing the desired task. This thesis presents the design, analysis, and realization of a dual-nacelle tiltrotor unmanned aerial vehicle. The design of the dual-nacelle tiltrotor aerial vehicle utilizes two propellers for thrust with the ability to rotate the propellers about the sagittal plane to provide thrust vectoring. The dual-nacelle thrust vectoring of the aerial vehicle provides a slimmer profile, a smaller hover footprint, and allows for rapid aggressive maneuvers while maintaining a desired speed to quickly navigate through cluttered environments. The dynamic model of the dual-nacelle tiltrotor design was derived using the Newton-Euler method and a nonlinear PD controller was developed for spatial trajectory tracking. The dynamic model and nonlinear PD controller were implemented in MATLAB® Simulink using SimMechanics. The simulation verified the ability of the controlled tiltrotor to track a helical trajectory. To study the scalability of the design, two prototypes were developed: a micro scale tiltrotor prototype, 50mm wide and weighing 30g, and a large scale tiltrotor prototype, 0.5m wide and weighing 2.8kg. The micro scale tiltrotor has a 1.6:1 thrust to weight ratio with an estimated flight time of 6 mins in hover. The large scale tiltrotor has a 2.3:1 thrust to weight ratio with an estimated flight time of 4 mins in hover. A detailed realization of the tiltrotor prototypes is provided with discussions on mechanical design, fabrication, hardware selection, and software implementation. Both tiltrotor prototypes successfully demonstrated hovering, altitude, and yaw maneuvering while tethered and remotely controlled. The developed prototypes provide a framework for further research and development of control strategies for the aggressive maneuvering of underactuated tiltrotor aerial vehicles.

**Acknowledgments**

First and foremost I would like to thank my advisor, Professor Stephen S. Nestinger. Your continued patience and guidance has not only made this project a reality but many, many others. As a true friend whether it be late at night or early in the morning you have helped me push through the most difficult challenges I have yet to face. Your guidance has helped me grow as person and changed my life for the better. I can never thank you enough.

Next I would like to thank my committee members, Dr. Gregory Fischer and Professor Cagdas Onal. I greatly appreciate the extra time you have spent guiding me through my collegiate career. Your help has improved my coursework and carried over to my projects. Your suggestions are always well thought out and give me a new perspective on ways to approach my projects.

To my group partner and best friend Siamak, you have pushed me to learn things I never would have attempted on my own. I can now confidently draw and model the dynamics of a two link arm without fear. Thank you for always being there, always willing to put my needs before your own, and refusing to walk through any thresh hold before me, your stubbornness will never be forgotten. I wish you all the best in your endeavors and I know I'll be seeing your name atop the most well known dynamics book within a few short years.

To my family, without your continued support, your kind words, and your steadfast examples of hard work, I would have never pushed myself nearly as hard as I did. To my aunt Robin, all of my projects, science fair success, and engineering related coursework are a tribute to you. Your perseverance, to get me to work for just 30 minutes longer, has given me a love and appreciation for the field of Engineering, and a passion in life.

To my friends who have helped me throughout my collegiate career with suggestions for designs, testing, and ways to improve myself personally I am forever indebted. Ross the late night lab adventures and the daily gym workouts have been some of the best times of my life. Vadim, your hard work and raw talent convinced me that a masters degree was easy, you lied. Colin you have continued to be one of my closest friends showing up at the drop of the hat for any help or support that I might need I can't imagine a better friend. Jon, you've always been a great friend, willing to go out of your way to help me whenever you can, JBJ. Ennio the early morning breakfast after an all-nighter always tastes the best. Brennan despite being 3,000 miles away, yet again you've had a helping hand in another project of mine.

Finally thank you Tracey. You are easily one of my favorite people on campus. No matter how much work I send your way, how many ridiculous requests I submit, you always greet me with a smile. I'm convinced there isn't another person in the world that could do what you do and this school is a better place because you are here.

# Contents

# List of Figures

# List of Tables

# List of Notations

| | |
|---|---|
| MB | Main Body |
| RTM | Right Tilting Mechanism |
| LTM | Left Tilting Mechanism |
| RP | Right Proprotor |
| LP | Left Proprotor |
| CR1 | Right joint connection point 1 |
| CL1 | Left joint connection point 1 |
| CR2 | Right joint connection point 2 |
| CL2 | Left joint connection point 2 |
| $M$ | Total mass of the robot |
| $m_b$ | Mass of MB |
| $m_{tR}$ | Mass of the RTM |
| $m_{tL}$ | Mass of the LTM |
| $m_{PR}$ | Mass of the RP |
| $m_{PL}$ | Mass of the LP |
| $I$ | Total Inertia matrix of the robot |
| $J_b$ | Inertia matrix of the main body |
| $J_{tR}$ | Inertia matrix of the RTM |
| $J_{tL}$ | Inertia matrix of the LTM |
| $J_{PR}$ | Inertia matrix of the RP |
| $J_{PL}$ | Inertia matrix of the LP |
| $V_i$ | Linear velocity |
| $\Omega$ | Angular velocity |
| $\theta_R$ | Rotation angle of the RTM w.r.t the MB |
| $\theta_L$ | Rotation angle of the LTM w.r.t the MB |
| $\omega_R$ | Angular velocity of the right prop w.r.t the RTM |
| $\omega_L$ | Angular velocity of the left prop w.r.t the LTM |
| $\overline{r}_R$ | Distance from C.G. of the MB to the CR1 |

| | |
|---|---|
| $\overline{r}_L$ | Distance from C.G. of the MB to the CL1 |
| $\overline{u}_R$ | Distance from C.G. of the RTM to the CR1 |
| $\overline{u}_L$ | Distance from C.G. of the LTM body to the CL1 |
| $\overline{v}_R$ | Distance from C.G. of the RTM to the CR2 |
| $\overline{v}_L$ | Distance from C.G. of the LTM to the CL2 |
| $\overline{w}_R$ | Distance from C.G. of the RP to the CR2 |
| $\overline{w}_L$ | Distance from C.G. of the LP to the CL2 |
| $\overline{d}_H$ | Distance from C.G. of the system to the center of the T frame |
| $\overline{d}_R$ | Distance from C.G. of the system to the center of the right propeller |
| $\overline{d}_L$ | Distance from C.G. of the system to the center of the left propeller |
| $\tau_{PR}$ | Driving torque of the RP |
| $\tau_{PR}$ | Driving torque of the LP |
| $\tau_{tR}$ | Driving torque of the RTM |
| $\tau_{tL}$ | Driving torque of the LTM |
| $\tau_{iL}$ | The induced aerodynamic moment acting on RP |
| $\tau_{iL}$ | The induced aerodynamic moment acting on LP |
| $f_{PR}$ | The thrust generated by the right propeller |
| $f_{PL}$ | The thrust generated by the left propeller |

# Chapter 1

# Introduction

Unmanned Aerial Vehicles (UAVs) have become more ubiquitous in research and industry over the last decade due to the advancement of materials and energy storage, and the miniaturization of computational, actuation, and sensing technology [1]. UAVs are used in a wide array of applications including, but not limited to, surveying mountain hazards [2], intelligence gathering, surveillance [3], search-and-rescue [4], first response, urban warfare, and wireless sensor networks [5]. Based on their requirements and performance specifications, UAVs vary in shape and size ranging from large dirigibles [6] and drones [7] to micro multi-rotor vehicles [8], helicopters [9], and ornithopters [10]. Figure 1.1 Under certain scenarios, such as first response and urban warfare, the agility, maneuverability and speed of the UAV are vital components towards the saving of human lives, successfully completing a mission, or stopping dangerous threats. Hence, slow yet efficient, dirigibles would not be suitable for rapidly maneuvering through cluttered environments. Under these circumstances, a high speed, highly agile, and small footprint unmanned

[1] http://www.blogcdn.com/www.engadget.com/media/2012/12/robots-ease-slider-01-04-12-12-02.jpg

[2] http://www.avinc.com/

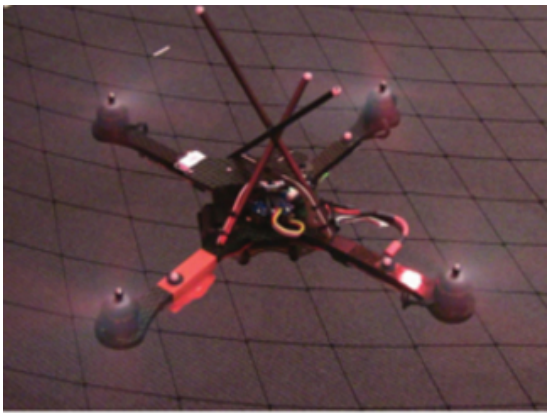

(a) A commercially available research quadrotor platform [8]

(b) Cyphyworks' EASE aerial vehicle navigating an urban setting. [1]

(c) Autonomous hovering of a fixed-wing micro aerial vehicle.[11]

(d) The AeroVironment flapping based hummingbird. [2]

Figure 1.1: Current research and consumer available UAV platforms

aerial vehicle capable of carrying minimal payloads would be the best suited design for completing the desired task. Although standard fixed wing aerial vehicles have demonstrated rapid and efficient motion, they typically operate at high speeds, are unable to hover in place, and have difficulty maneuvering through cluttered environments such as damaged buildings. Equipped with high static thrust propellers and an appropriate controller, fixed wing UAVs, such as the aircraft shown in Figure 1.1c, have demonstrated hover capability with limited maneuverability [11]. Recent research has focused on propeller driven aerial "wingeron" vehicles capable of actuating entire wing surfaces to enhance system response [12]. These systems are highly agile and are shown to execute knife edge maneuvers to quickly change orientation while navigating through densely populated environments at high speeds. However, the system is incapable of hover or slow motion movements which are necessary for current mapping practices. Generally, these fixed wing systems are incapable of vertical takeoff and landing (VTOL).

Ornithopters are bio-inspired aerial vehicles that mimic the motion of birds and insects for flight. These systems have received increased attention in recent years utilizing wing flapping and feathering techniques to produce unusually high lift [10, 13] in micro aerial vehicles (MAV). They have shown promise with regards to efficient long distance flight but only a few are capable of hover or VTOL. The most notable and capable ornithopter is the hummingbird [14] developed in cooperation with the United States Defense Advanced Research Projects Agency (DARPA) as a surveillance platform that exhibits life like motion. Despite continued and longstanding research, ornithopters are still limited in payload and speed.

For higher payload capability and faster flight in VTOL applications, aerial vehicle research has turned to the development of quad-rotors and any variation thereof typically referred to as N-rotors [8]. Similar research efforts to improve air-

craft yaw control, agility and durability have developed tri-rotors [15], dual rotors, and single rotor systems [16]. In general, these systems are under actuated and exhibit complex dynamics requiring outside observation to provide adequate sensing to control the system. Attempts have been made to provide full system controllability by adding additional DoF to quad-rotors [17, 18]. However, these mechanical solutions increase the dimensionality of the state space and complicate the control system. Quad-rotors also require a large hover footprint and the need for aggressive maneuvers to pass through narrow vertical passage ways.

The concept of a tiltrotor aerial vehicles has been researched before in simulation and realized physical systems. A. Sanchez et al. [19] were able to design and realize a physical tiltrotor system capable of sustained hover using simplified dynamic equations and decoupled control laws for maintaining lateral, longitudinal, and axial dynamics. Following this investigation, Christos Papachristos et al. discussed the development of tiltrotor aerial vehicles as a viable platform for autonomous search and rescue operations [20]. The work presented a modular architecture for robotic control specifically designed for unconventional unmanned vehicle systems. More recent work into the development of a model predictive attitude control scheme [21] and an open source research platform [22] suggest a continued interest in the use of tiltrotors aerial vehicles to combine the maneuverability of helicopters with long distance flight of fixed wing aircraft [23].

This thesis presents the design, analysis, and realization of a dual-nacelle tiltrotor unmanned aerial vehicle shown in Figure 1.2. The proposed system utilizes two nacelle units for thrust. The aircraft has the ability to rotate the thrust output about the sagittal plane providing controllable system thrust vectoring. Hence, the dual-nacelle tiltrotor provides a narrow hovering footprint with otherwise similar characteristics to other available unmanned aerial vehicles. The thrust vectoring of

Figure 1.2: The proposed dual-nacelle tiltrotor concept aerial vehicle

the aerial vehicle allows for rapid aggressive maneuvers while maintaining a desired speed to quickly navigate through cluttered environments. The platform is designed to facilitate the benefits of both a fixed wing aircraft and that of a VTOL helicopter platform. To do this, the platform exhibits the benefit of stable and efficient hover with the ability to transition fluidly into a horizontal orientation for high speed translations.

## 1.1 Thesis Contributions

The main objective of this thesis is the analysis and realization of two dual-nacelle tiltrotors. These platforms are designed for future research on the development of advanced controller strategies for aggressive maneuvers of underactuated aerial vehicles. Presented are two realizations of the dual-nacelle tiltrotor design, a full scale and micro scale variant. The micro scale design allows for in-door testing

with enhanced safety while the full scale design allows for out-door testing and more aggressive flight maneuvers. In achieving the desired thesis objective, the contributions of the thesis are as follows:

- A study on the feasibility of the control and realization of a dual-nacelle tiltrotor aerial vehicle for aggressive maneuvering within cluttered and close-quarters environments was completed. The study focused on the scalability of the dual-nacelle tiltrotor design with regards to desired performance metrics including, flight duration and thrust.

- A multi-body dynamic model of a dual-nacelle tiltrotor aerial vehicle was derived based on the Newton-Euler method for use in control and simulation. A simplified dynamic model of a dual-nacelle tiltrotor was also derived for the aerial vehicle system utilizing a single body approach to simplify the control implementation. A MATLAB® Simulink block was implemented based on the dynamic model of a dual-nacelle tiltrotor. The Simulink block was used to simulate the dual-nacelle tiltrotor, verify control strategies, and tune control parameters.

- A non-linear PD attitude and altitude controller was designed the dual-nacelle tiltrotor based on the simplified derived dynamic model. The non-linear PD controller was verified in simulation using the implemented MATLAB® Simulink block. The implemented MATLAB® Simulink block was augmented to include a realistic model of the tilting servo through the consideration of the control dynamics of the internal servo P controller and a model of the the system response delay due to the PWM output frequency of 50Hz using a zero-hold. The simulation verified that the controlled dual-nacelle tiltrotor was able to track a spacial helix trajectory. The simulation was used to tune the controller

parameters based on the realized system dynamics and physical properties.

- Two dual-nacelle tiltrotor prototypes were designed and realized. The prototypes consisted of a 0.5m wide, 2.8kg full scale tiltrotor and a 50mm wide, 30g micro scale tiltrotor. An in-depth description of the realization process is provided including component and material selection, and implementation methods.

- An in-depth analysis of the propeller and ducted fan performance is completed. The thrust curves and power curves for both systems were measured and categorized. The thrust versus PWM signal for the motor controller and propeller combinations was generated along with the thrust versus PWM signal for the ducted fans.

- Experimental demonstration of both tiltrotors in hover is presented. The hovering capability of both tiltrotor prototypes was demonstrated through tethered operation. The demonstration indicates that both prototypes are capable of producing sufficient thrust to maintain hover and increase altitude.

- Discussion on the design and scalability considerations for dual-nacelle tiltrotor aerial vehicles.

## 1.2 Thesis Layout

The remaining chapters of the thesis are outlined as follows. Chapter 2 presents a model of the tiltrotor aerial vehicle where the parameters specific to the proposed design are used to derive the equations of motion using Newton-Euler dynamics. Chapter 3 outlines the creation and implementation of a non-linear PD controller for

the system. The system, controller, and environment are modeled in MATLAB® using SimMechanics and Simulink. The simulation allows for initial coarse, and future fine, tuning of the controller gains before implementation on real hardware. Chapter 4 presents an in-depth analysis of the design process, design parameters, component selection, and manufacturing of the two realized systems. Chapter 5 describes the system validation including the analysis of the system results. Chapter 6 Makes recommendations to future work for the project, including the development of a new micro tiltrotor. Conclusions are drawn at the end of Chapter 7.

# Chapter 2

# Model of a Dual-Nacelle Tiltrotor

This chapter presents a description of the dual-nacelle tiltrotor followed by a derivation of the mathematical model for use in simulation and control. The dynamic model of the aerial vehicle was generated using the Newton-Euler method. The following sections discuss the approach to modeling of each sub-component of the system and the equations of motion for the full system.

## 2.1 Description of the Dual-Nacelle Tiltrotor

The dual-nacelle tiltrotor aerial vehicle contains two thrust generating nacelles attached to the main body via rotational joints. An example of a dual-nacelle tiltrotor aerial vehicle is given in Figure 2.1. From 2.1, the system can be broken up into five articulated bodies: the Main Body (MB), the Right Tilting Mechanism (RTM), the Left Tilting Mechanism (LTM), the Right Proprotor (RP), and the Left Proprotor (LP).

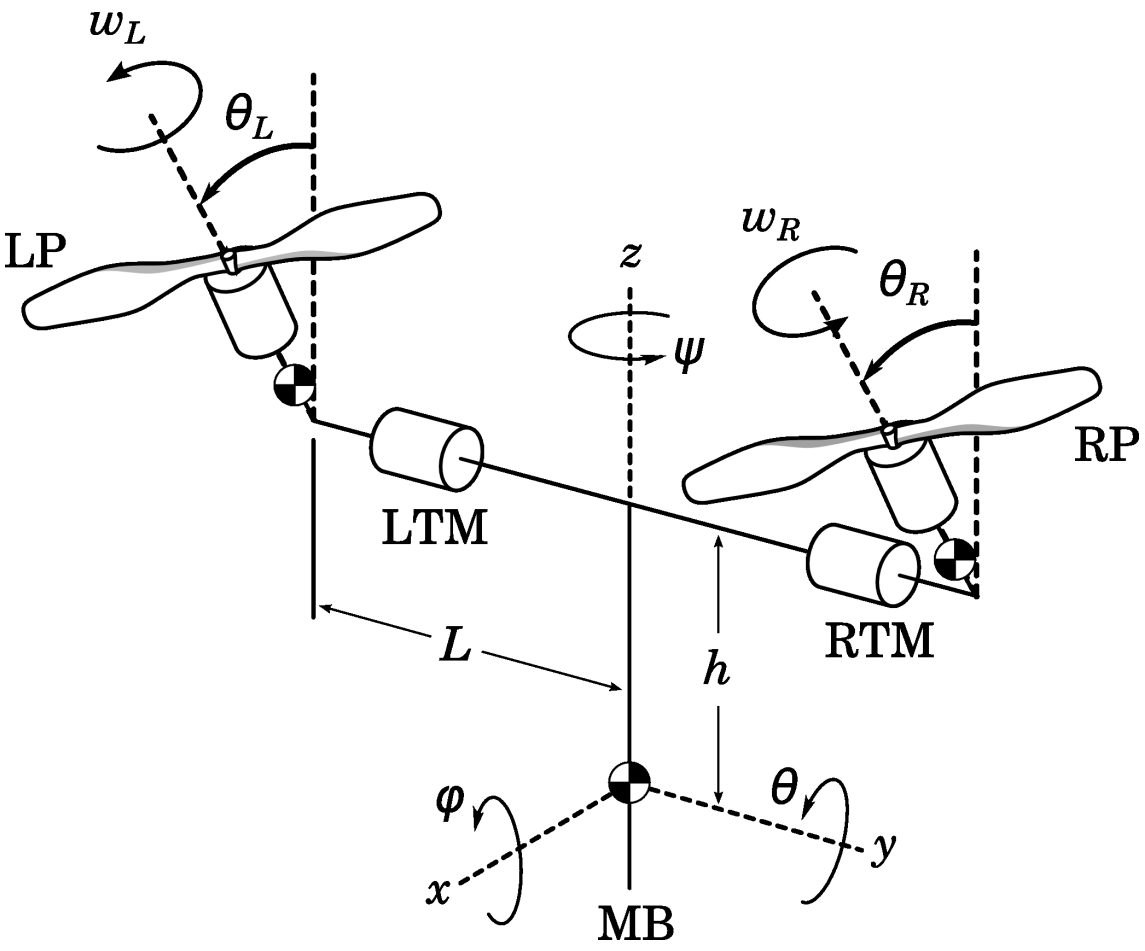


Figure 2.1: The kinematic representation of a tiltrotor aircraft for parameter identification.

## 2.2 Dynamic Model of the Dual-Nacelle Tiltrotor

The simplified kinematic structure of the full system is depicted in Figure 2.2. The notations used to derive the dynamic model of the system follow the format used in [24], where: ${}^{j}x_i$ represents the vector $x_i$ defined in coordinate system $\{j\}$ and ${}^{j}_{i}R$ is the rotation matrix that maps the coordinate system $\{i\}$ to $\{j\}$. All of the parameters used in the this section are introduced in Figure 2.1, Figure 2.2, and a comprehensive list is outlined in the List of Notations.

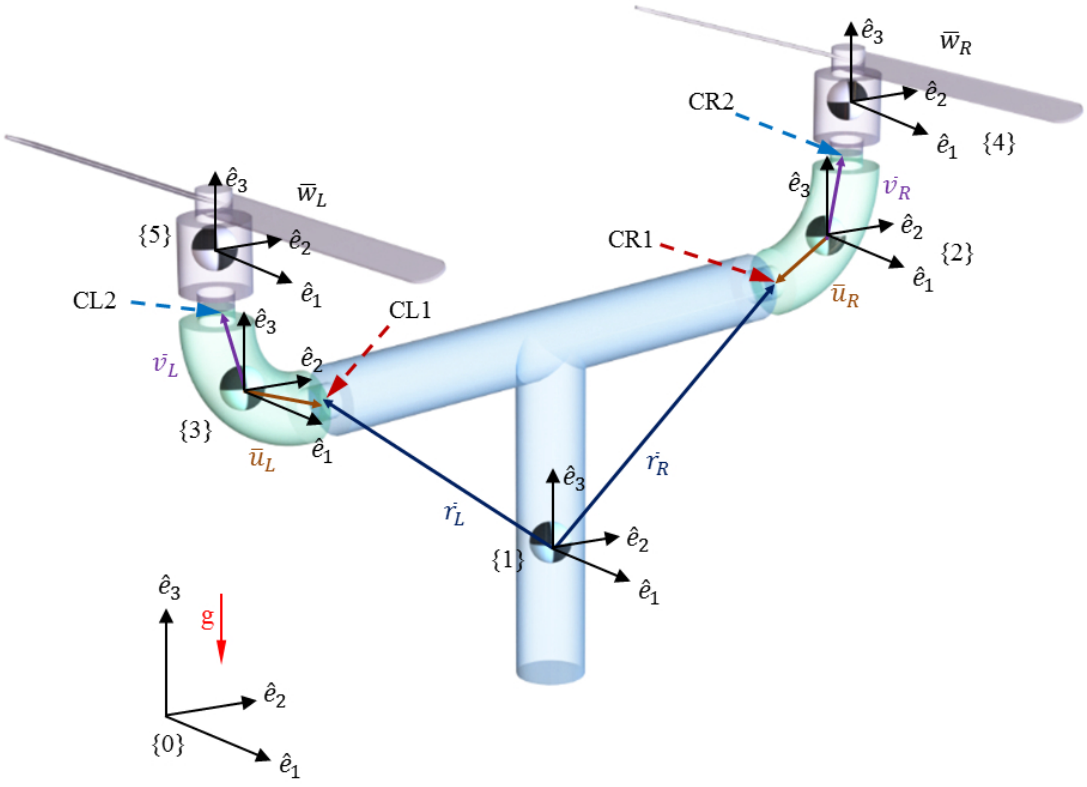


Figure 2.2: A simplified visual representation of the tiltrotor aerial vehicle

### 2.2.1 Proprotor Model

The free-body diagram of the RP is illustrated in Figure 2.3. The Newton-Euler formulations for this section of the robot, in a body fixed coordinate frame {4} are described in Equations (2.1) and (2.2).

$$m_{PR}{}^4\dot{V}_4 = -m_{PR}{}^4\Omega_4 \times {}^4V_4 + m_{PR}g({}^4_0R \cdot \hat{e}_3) + {}^4\overline{F}_{24} + f_{PR} \cdot \hat{e}_3 \tag{2.1}$$

$$J_{PR}{}^4\dot{\Omega}_4 = -{}^4\Omega_4 \times J_{PR}{}^4\Omega_4 + {}^4\overline{M}_{24} + (\tau_{PR} - \tau_{iR}) \cdot \hat{e}_3 + \overline{w}_R \times ({}^4\overline{F}_{24} + f_{PR} \cdot \hat{e}_3) \tag{2.2}$$

where $m_{PR}$ is the mass, $f_{PR}$ is the thrust produced by the prop, $J_{PR}$ is the inertia matrix of the RP, $\tau_{PR}$ is the driving torque, $\tau_{iR}$ is the induced aerodynamic moment of the RP $\overline{w}_R$ is the distance from the C.G. of the system to the center of the RP, and ${}^4\overline{F}_{24}$ and ${}^4\overline{M}_{24}$ are the reaction (joint) forces and moments respectively, of the

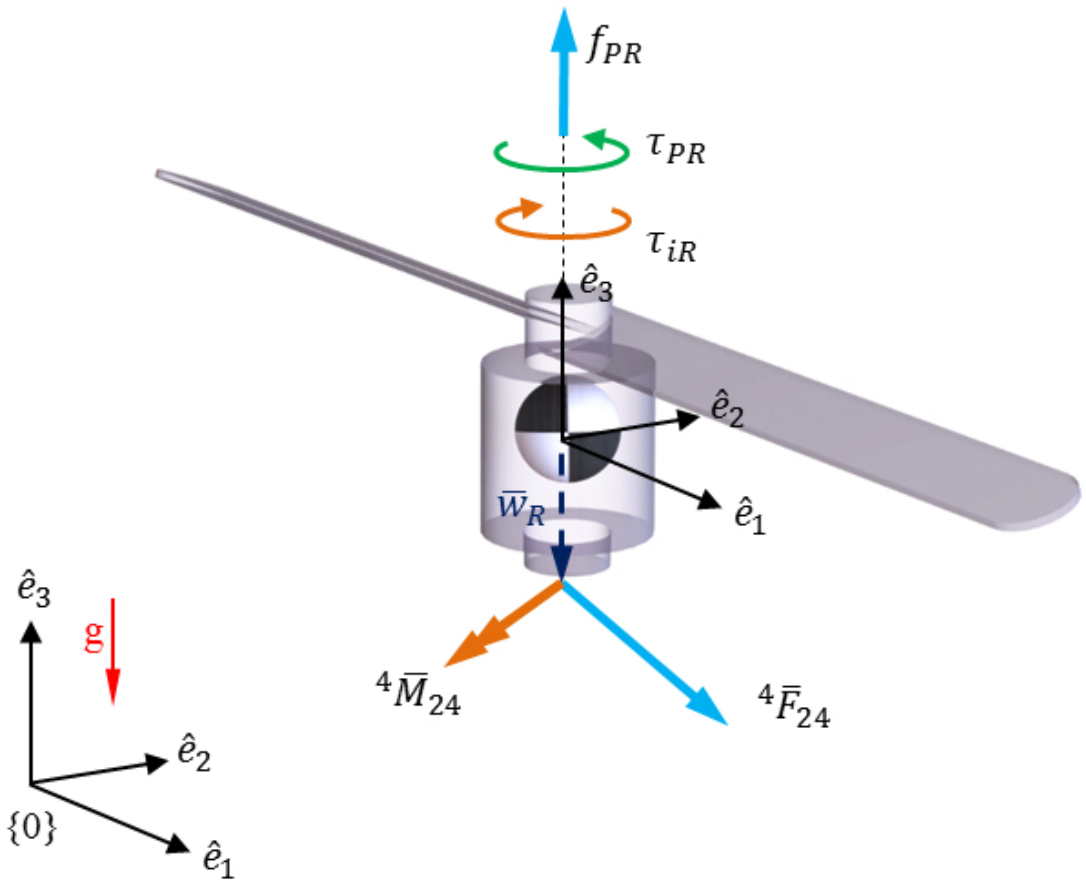


Figure 2.3: A simplified model of the thrust motor.

right joint connection point 2 (CR2) that are defined in coordinate system {4}. ${}^4\overline{F}_{24}$ and ${}^4\overline{M}_{24}$ are defined by Equations (2.3) and (2.4), respectively:

$$ {}^4\overline{F}_{24} = F_{x_{24}} \cdot \hat{e}_1 + F_{y_{24}} \cdot \hat{e}_2 + F_{z_{24}} \cdot \hat{e}_3 \tag{2.3} $$

$$ {}^4\overline{M}_{24} = M_{x_{24}} \cdot \hat{e}_1 + M_{y_{24}} \cdot \hat{e}_2 \tag{2.4} $$

$$ f_{PR} = k_f \cdot w^2 \tag{2.5} $$

$$ \tau_{iR} = k_t \cdot w \tag{2.6} $$

### 2.2.2 Tilt-motor Model

The free-body diagram of the RTM is depicted in Figure 2.4. The corresponding Newton-Euler formulations for this section of the system are described in Equations, defined in the body fixed coordinate frame {2} (2.7) and (2.8).

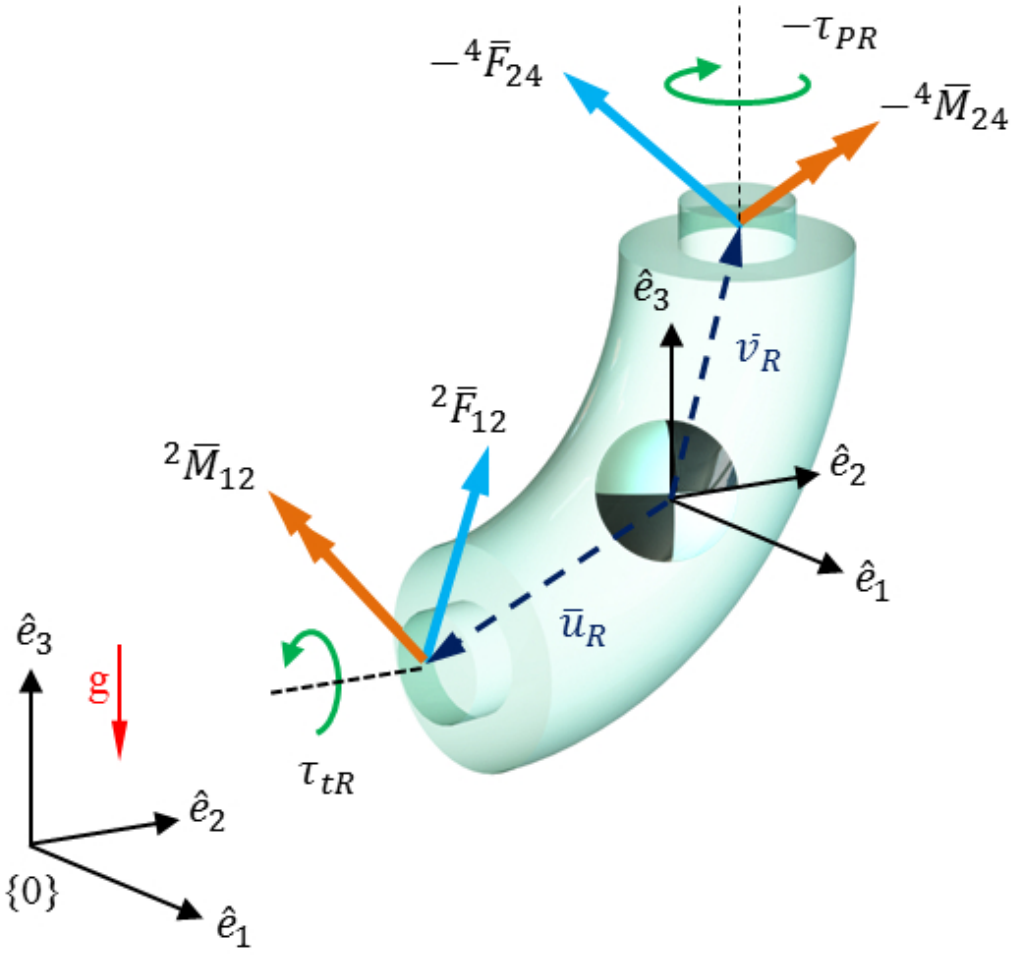


Figure 2.4: A simplified model of the tilting mechanism.

$$m_{tR}{}^2\dot{V}_2 = -m_{tR}{}^2\Omega_2 \times^2 V_2 + m_{tR}g({}^2_0R \cdot \hat{e}_3) + {}^2\overline{F}_{12} - {}^2_4R^4\overline{F}_{24} \tag{2.7}$$

$$\begin{aligned} J_{tR}{}^2\dot{\Omega}_2 = &-{}^2\Omega_2 \times J_{tR}{}^2\Omega_2 - {}^2_4R({}^4\overline{M}_{24} - \tau_{PR} \cdot \hat{e}_3) + {}^2\overline{M}_{12} \\ &+ \tau_{tR} \cdot \hat{e}_2 + {}^2\overline{u}_R \times {}^2\overline{F}_{12} - {}^2\overline{v}_R \times {}^2_4R^4\overline{F}_{24} \end{aligned} \tag{2.8}$$

where $m_{tR}$ is the mass, $J_{tR}$ is the inertia matrix of the RTM, $\tau_{tR}$, is the driving torque of the RTM $\overline{u}_R$ is the distance from the C.G. of the RTM to the CR1, and $\overline{v}_R$ is the distance from the C.G. of the RTM to the CR2. ${}^2\overline{F}_{12}$ and ${}^2\overline{M}_{12}$ are defined by Equations (2.9) and (2.10), respectively:

$$ {}^2\overline{F}_{12} = F_{x_{12}} \cdot \hat{e}_1 + F_{y_{12}} \cdot \hat{e}_2 + F_{z_{12}} \cdot \hat{e}_3 \tag{2.9} $$

$$ {}^2\overline{M}_{12} = M_{x_{12}} \cdot \hat{e}_1 + M_{z_{12}} \cdot \hat{e}_3 \tag{2.10} $$

In a similar fashion, one can formulate the Newton-Euler equations for the LP and LTM following the same convention. The corresponding Equations are derived in (2.11) to (2.18).

$$ m_{PL}\,{}^5\dot{V}_5 = -m_{PL}\,{}^5\Omega_5 \times {}^5V_5 + m_{PL}g({}^5_0R \cdot \hat{e}_3) + {}^5\,\overline{F}_{35} + f_{PL} \cdot \hat{e}_3 \tag{2.11} $$

$$ J_{PL}\,{}^5\dot{\Omega}_5 = -{}^5\Omega_5 \times J_{PL}\,{}^5\Omega_5 + {}^5\overline{M}_{35} + (\tau_{PL} - \tau_{iL}) \cdot \hat{e}_3 + \overline{w}_L \times ({}^5\overline{F}_{35} + f_{PL} \cdot \hat{e}_3) \tag{2.12} $$

$$ m_{tL}\,{}^3\dot{V}_3 = -m_{tL}\,{}^3\Omega_3 \times {}^3\,V_3 + m_{tL}g({}^3_0R \cdot \hat{e}_3) + {}^3\overline{F}_{13} - {}^3_5R\,{}^5\overline{F}_{35} \tag{2.13} $$

$$ \begin{aligned} J_{tL}\,{}^3\dot{\Omega}_3 = {} & -{}^3\Omega_3 \times J_{tL}\,{}^3\Omega_3 - {}^3_5R({}^5\overline{M}_{35} - \tau_{PL} \cdot \hat{e}_3) + {}^3\overline{M}_{13} \\ & + \tau_{tL} \cdot \hat{e}_2 + {}^3\overline{u}_L \times {}^3\overline{F}_{12} - {}^3\overline{v}_L \times {}^3_5R\,{}^5\overline{F}_{35} \end{aligned} \tag{2.14} $$

$$ {}^5\overline{F}_{35} = F_{x_{35}} \cdot \hat{e}_1 + F_{y_{35}} \cdot \hat{e}_2 + F_{z_{35}} \cdot \hat{e}_3 \tag{2.15} $$

$$ {}^5\overline{M}_{35} = M_{x_{35}} \cdot \hat{e}_1 + M_{y_{35}} \cdot \hat{e}_2 \tag{2.16} $$

$$ {}^3\overline{F}_{13} = F_{x_{13}} \cdot \hat{e}_1 + F_{y_{13}} \cdot \hat{e}_2 + F_{z_{13}} \cdot \hat{e}_3 \tag{2.17} $$

$$ {}^3\overline{M}_{13} = M_{x_{13}} \cdot \hat{e}_1 + M_{z_{13}} \cdot \hat{e}_3 \tag{2.18} $$

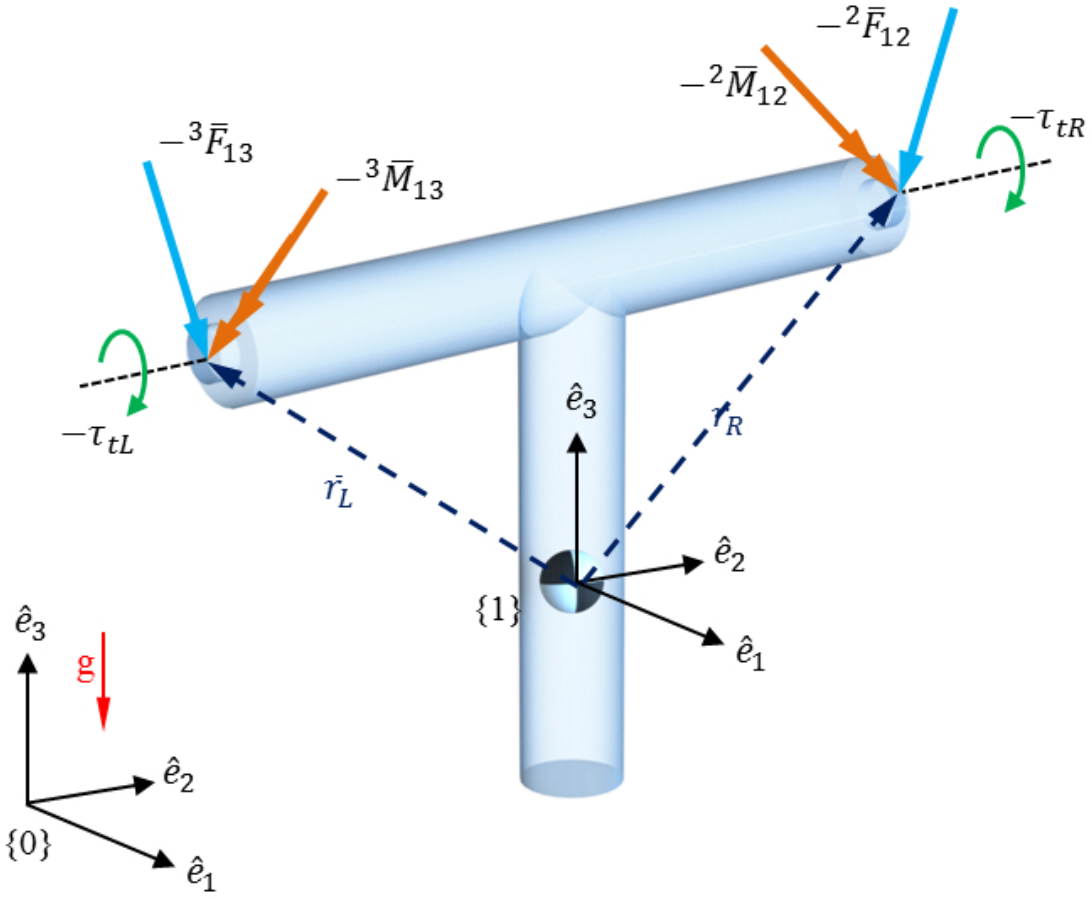


Figure 2.5: A simplified model of the main tiltrotor body.

### 2.2.3 Main Body Model

The free-body diagram of the MB is depicted in Figure 2.5. The Newton-Euler formulations for the MB defined in the body fixed coordinate frame $\{1\}$ given as Equations (2.19) and (2.20):

$$m_b {}^1\dot{V}_1 = -m_b {}^1\Omega_1 \times {}^1V_1 + m_b g({}^1_0R \cdot \hat{e}_3) - {}^1_2R {}^2\overline{F}_{12} - {}^1_3R {}^3\overline{F}_{13} \tag{2.19}$$

$$\begin{aligned} J_b {}^1\dot{\Omega}_1 = &-{}^1\Omega_1 \times J_b {}^1\Omega_1 - {}^1_2R({}^2\overline{M}_{12} + \tau_{tR} \cdot \hat{e}_2) \\ &- {}^1_3R({}^3\overline{M}_{13} + \tau_{tL} \cdot \hat{e}_2) - {}^1\overline{r}_R \times {}^1_2R {}^2\overline{F}_{12} - {}^1\overline{r}_L \times {}^1_3R {}^3\overline{F}_{13} \end{aligned} \tag{2.20}$$

where $m_b$ is the mass of the main body, $J_b$ is the inertia matrix of the body, and $\overline{r}_R$ is the distance from the C.G. to the main body of CR1.

### 2.2.4 Simplified Single Body Model

It is possible to further simplify the governing dynamic equations of the system by approximating it with a single body. To do so, it is assumed that the center of mass of the RTM, LTM, RP, and LP lay along the line of actuation of the CR1 and CL1. Thus it is possible to write the forces and moments of the robot about the center of mass of the whole system, since the values of $\theta_R$ and $\theta_L$ have no affect on the position of the C.G. in either the RTM or the LTM. Assuming that the propellers of both the LP and RP are rotating at relatively large angular velocities, the corresponding gyroscopic effects should be considered. The Newton-Euler equations for the simplified model of the robot, defined in the body fixed coordinate frame $\{1\}$ are described in Equations (2.21) and (2.22):

$$M\,{}^1\dot{V}_1 = -M\,{}^1\Omega_1 \times {}^1V_1 + Mg({}^2_0R \cdot \hat{e}_3) + f_{PR}({}^1_2R \cdot \hat{e}_3) + f_{PL}({}^1_3R \cdot \hat{e}_3) \quad (2.21)$$

$$\begin{aligned} I\,{}^1\dot{\Omega}_1 = &-{}^1\Omega_1 \times I\,{}^1\Omega_1 + f_{PR}({}^1\overline{d}_R \times {}^1_2R \cdot \hat{e}_3) + f_{PL}({}^1\overline{d}_L \times {}^1_3R \cdot \hat{e}_3) \\ &+ ({}^1\Omega_1 + \dot{\theta}_R \cdot \hat{e}_2) \times J_{PR}({}^1\Omega_1 + \dot{\theta}_R \cdot \hat{e}_2 + {}^1_2R\omega_{PR_z} \cdot \hat{e}_3) \\ &+ ({}^1\Omega_1 + \dot{\theta}_L \cdot \hat{e}_2) \times J_{PL}({}^1\Omega_1 + \dot{\theta}_L \cdot \hat{e}_2 + {}^1_3R\omega_{PL_z} \cdot \hat{e}_3) \end{aligned} \quad (2.22)$$

$${}^0_1\dot{R} = {}^0_1R \cdot \text{Skew}({}^1\Omega_1) \quad (2.23)$$

$${}^0V_1 = {}^0_1R\,{}^1V_1 \quad (2.24)$$

where $M$ is the total mass of the robot, $I$ is the total inertia matrix of the robot, and $\omega_{PR}$ and $\omega_{PL}$ are the angular velocities of the left and right propeller with respect to the left and right tilting mechanisms. The dynamic response of the

tilting mechanism and thruster can be approximated by Equations (2.25), (2.26), (2.27), and (2.28):

$$J_{PR_{zz}}\dot{\omega}_R = \tau_{PR} - \tau_{iR} \tag{2.25}$$

$$J_{tR_{yy}}\ddot{\theta}_R = \tau_{tR} + [({}^1\Omega_1 + \dot{\theta}_R \cdot \hat{e}_2)\times J_{PR}({}^1\Omega_1 + \dot{\theta}_R \cdot \hat{e}_2 + \tfrac{1}{2}R\omega_R \cdot \hat{e}_3)] \cdot \hat{e}_2 \tag{2.26}$$

$$J_{PL_{zz}}\dot{\omega}_L = \tau_{PL} - \tau_{iL} \tag{2.27}$$

$$J_{tL_{yy}}\ddot{\theta}_L = \tau_{tL} + [({}^1\Omega_1 + \dot{\theta}_L \cdot \hat{e}_2)\times J_{PL}({}^1\Omega_1 + \dot{\theta}_L \cdot \hat{e}_2 + \tfrac{1}{3}R\omega_L \cdot \hat{e}_3)] \cdot \hat{e}_2 \tag{2.28}$$

where the the system states $\overline{x}$, and the system control inputs $\overline{u}$ are defined as:

$$\overline{x} = \begin{bmatrix} x & y & z & \dot{x} & \dot{y} & \dot{z} & \theta & \phi & \psi & \dot{\theta} & \dot{\phi} & \dot{\psi} & \theta_R & \theta_L & \dot{\theta_R} & \dot{\theta_L} & \omega_R & \omega_L \end{bmatrix}^T \tag{2.29}$$

$$\overline{u} = \begin{bmatrix} \tau_{PR} & \tau_{PL} & \tau_{tR} & \tau_{tL} \end{bmatrix}^T \tag{2.30}$$

Note that $\theta$, $\phi$, and $\psi$ are not directly observable from the state equations.

### 2.2.5 Parameter Identification

| Parameter Name | Value | Method of Identification |
|---|---|---|
| Mass | 2.81kg | Measured |
| Robot Width | 0.58m | Measured |
| Robot Height | 0.30m | Measured |
| Robot Depth | 0.13m | Measured |
| Nacelle Mass | 0.53kg | Measured |
| Maximum Nacelle $f_P$ | 3.2kg | Data Sheet |
| Maximum Nacelle $\omega$ | 5.00Rad/sec | Data Sheet |
| Control Loop Rate | 50Hz | Calculated |

Table 2.1: Model Parameters. Parameters are either: measured directly, calculated from the SolidWorks® CAD model, or computed using known control laws.

Table 2.1 outlines the parameter values pertaining to the tiltrotor design and the method used for their identification. Further information regarding the

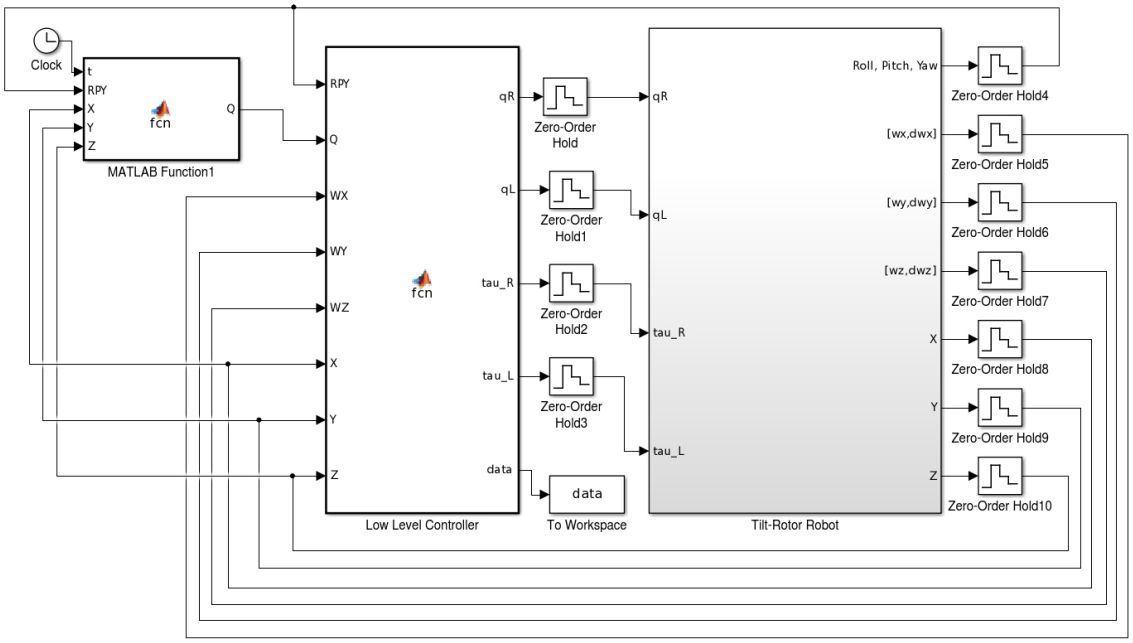


Figure 2.6: Simulink Model of the Simulation.

locations of the center of mass for the nacelle unit, the main body, as well as the fully assembled robot were calculated using the CAD model. Information regarding the moments of inertia of the aforementioned components were also calculated using the same CAD model.

## 2.3 MATLAB® SimMechanic Model

The complete simulation was constructed within Simulink as part of the MATLAB® software suite using multiple embedded levels to describe each of the simulation components. Figure 2.6 presents a block diagram of the top view of the simulation. The blocks represent the desired trajectory in world coordinates, the simplified PD robot controller, and the robot system. The diagram also displays the use of Zero-Order hold blocks which enable the delay of signals and state variables as to better model the real world system calculation and sensor sample delay. It is important to note

that the servos and the ESCs were purchased as off the shelf components and, as is typical with these component designs, there is no access to the feedback control for motor acceleration, motor torque, or motor velocity. However, these system responses were modeled as individual blocks in the simulation where the speed of the response best models the mechanical response of the electrical input. These responses are achieved through the use of PID controllers for the servos, brushless motor controllers a control loop time of 50Hz. These subsystem approximations are shown in Figure 2.7.

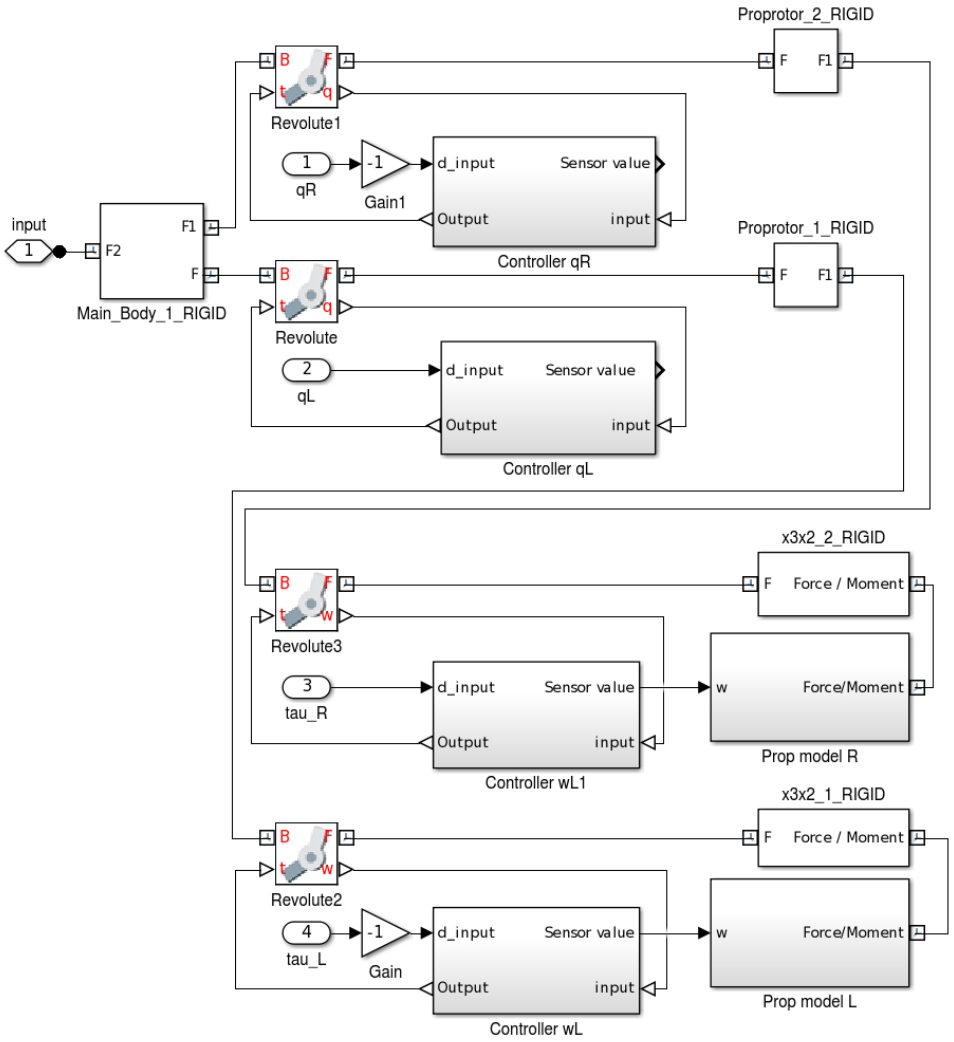


Figure 2.7: MATLAB® Simulink subsystem: tiltrotor subsystems model.

## 2.4 Summary

In summary this chapter has provided a comprehensive description of the tiltrotor design. The dynamic model of the dual-nacelle tiltrotor aerial vehicle was derived using the Newton-Euler method. This was approached through the modeling of each subsystem as an individual body, summing all the components together to arrive at a full system model. A simplified model of the system was created by generalizing the C.G. locations of the exterior components. An ideal tiltrotor simulation, based on real-world design specifications and constraints, was created. This simulation included approximated sensor, actuator, and control loop delay through the simulation of the internal controller, as well as the servo motors and ESCs response.

# Chapter 3

# Control of a Dual-Nacelle Tiltrotor Aerial Vehicle

The control of the tiltrotor aerial vehicle across smooth trajectories is challenging for several reasons [8]. First, the system is underactuated thus, the vehicle control inputs produce strongly coupled motion. Second, the dynamic model derived prior is an approximate and ideal representation of the aircraft. Finally, the system control inputs are modeled as an ideal instant response to control signals, without motor lag or propeller spin up delay.

## 3.1 Control Structure

Here a non-linear proportional controller, with derivative feedback, capable of stable flight in simulation is implemented. Figure 3.1 is a generalized block diagram depicting the control flow for the simulated and realized aerial robot. The system calculates a trajectory plan based on the desired relocation as measured in the world coordinate frame. These updated desired positions are distributed to both the posi-

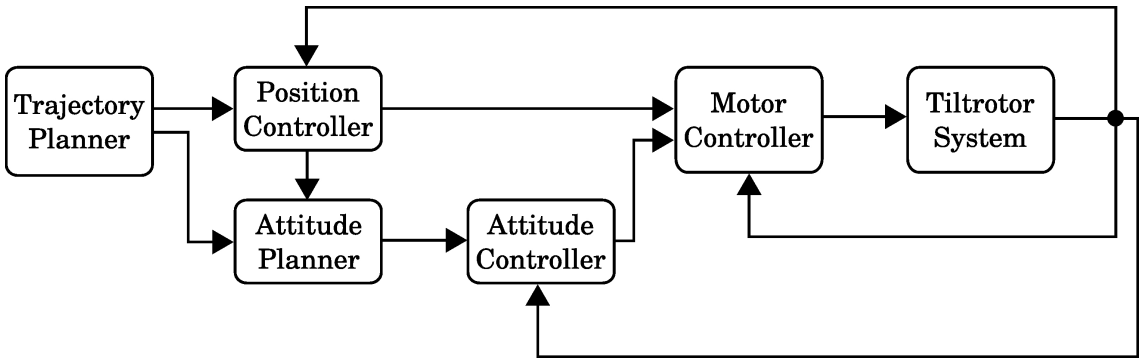


Figure 3.1: Generalized controller of an aerial vehicle for trajectory tracking.

tion controller as well as the attitude planner. Current and desired state information is passed to the attitude controller which generates a reference signal for the motor controller. The position and attitude controller outputs are mapped to the motor controllers resulting in a system response. The tiltrotor system observes the changes in the current state including the motor velocity, nacelle orientation, body position, and attitude in the world frame and redistributes the updated information to the position and attitude controllers. A detailed view of the control scheme used for the dual-nacelle tiltrotor is shown in Figure 3.2.

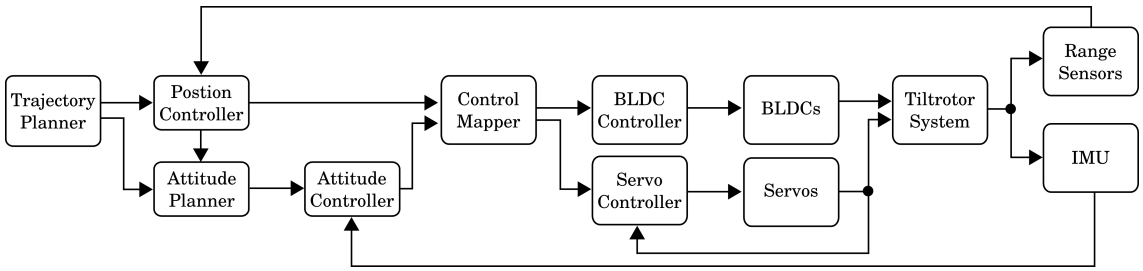


Figure 3.2: Detailed controller implementation for the dual-nacelle tiltrotor.

## 3.2 Control Mapping

The system control inputs for the aerial vehicle are the propeller velocities and their respective orientation to the body about the y-axis of the body fixed frame. Control of the flight path of the aircraft is difficult to visualize. Hence, a mapping has been derived from the simplified dynamics of the system, where, the desired forces and moments are calculated based on the control inputs. To simplify the system control equations the servo angular velocity $\dot{\theta}$, the servo angular acceleration $\ddot{\theta}$, and the propeller angular acceleration $\dot{\omega}$ are neglected. These assumptions are made due to the fact that servo motors and ESCs do not allow direct torque control. Based on the assumption, the new system states $\overline{x}$, and the system control $\overline{u}$ become:

$$\overline{x} = \begin{bmatrix} x & y & z & \dot{x} & \dot{y} & \dot{z} & \theta & \phi & \psi & \dot{\theta} & \dot{\phi} & \dot{\psi} \end{bmatrix}^T \tag{3.1}$$

$$\overline{u} = \begin{bmatrix} \theta_L & \theta_R & f_{PR} & f_{PL} \end{bmatrix}^T \tag{3.2}$$

The equations defining the motion of the aircraft are re-arranged to separate the control inputs from the rest of the system dynamics. Based on the equations outlined in Chapter 2, Equation (3.3) is derived by moving all of the system inputs to the right-hand side.

$$\begin{aligned} f_{PR} \cdot sin(\theta_R) + f_{PL} \cdot sin(\theta_L) &= F_x \\ f_{PR} \cdot cos(\theta_R) + f_{PL} \cdot cos(\theta_L) &= F_z \\ f_{PR} \cdot L \cdot cos(\theta_R) + f_{PL} \cdot L \cdot cos(\theta_L) &= M_x \\ f_{PR} \cdot h \cdot sin(\theta_R) + f_{PL} \cdot h \cdot sin(\theta_L) &= M_y \\ f_{PR} \cdot L \cdot cos(\theta_R) + f_{PL} \cdot L \cdot cos(\theta_L) &= M_z \end{aligned} \tag{3.3}$$

where $F_i$ and $M_i$ are the forces and moments, respectively, acting on the center of mass of the aerial vehicle along the $i$ direction due to the to $f_{PR}$ and $f_{PL}$ forces.

Equation 3.3 does not contain the dynamic equation for the motion in the y-axis since $F_y$ does not correlate to any system input. The system control inputs, $\theta_L$ and $\theta_R$ represent the angles describing the orientation of the LTM and RTM with respect to the MB, and $f_{PL}$ and $f_{PR}$ represent the thrust of the LP and RP. From Equation 3.3, the system has four control inputs and six degrees of freedom. Hence, the system is underactuated and contains highly coupled dynamics. Thus, there is no unique solution to map the desired forces and moments to the control inputs of the system. Using algebraic and trigonometric manipulation, a non-linear mapping of the desired body torques and forces to the system inputs can be derived as given in Equation 3.4.

$$\begin{aligned} f_{PR} &= 0.5 \cdot \sqrt{\left(\frac{M_z}{L} + \frac{M_y}{h}\right)^2 + \left(F_z - \frac{M_x}{L}\right)^2} \\ f_{PL} &= 0.5 \cdot \sqrt{\left(\frac{M_y}{h} - \frac{M_z}{L}\right)^2 \left(F_z + \frac{Mx}{L}\right)^2} \\ \theta_R &= atan2\left(\frac{M_z}{L} + \frac{M_y}{h}, F_z - \frac{M_x}{L}\right) \\ \theta_L &= atan2\left(\frac{M_y}{h} - \frac{M_z}{L}, F_z + \frac{M_x}{L}\right) \end{aligned} \tag{3.4}$$

## 3.3 Attitude and Altitude Control

A proportional controller with velocity feedback is utilized to control the roll, pitch, and altitude of the aerial vehicle while the yaw control is achieved by a velocity controller with acceleration feedback. The controller involves two constant parameters $K_P$ and $K_D$, a proportional and derivative gain, to provide control action based on the current and desired state of the system. The present state errors are observed using an on-board inertial measurement unit (IMU), an altimeter, and infrared range sensors for attitude, body accelerations, and altitude measurements respectively. From these measurements, the current system Euler angles are calcu-

lated using a direction cosine matrix. Whereas the expected future errors are based on the dynamic equations describing the system. The waited sum of these two actions are used to adjust the current input parameters in order to reduce the system state error. Equation (3.5) presents the implemented control laws for the system.

$$\begin{aligned} U_1 &= K_{p,\theta}(\theta_d - \theta) - K_{d,\theta}(\dot{\theta}) \\ U_2 &= K_{p,\phi}(\phi_d - \phi) - K_{d,\phi}(\dot{\phi}) \\ U_3 &= K_{p,\psi}(\psi_d - \psi) - K_{d,\psi}(\dot{\psi}) \\ U_4 &= K_{p,z}(z_d - z) - K_{d,z}(\dot{z}) + F_{hover} \end{aligned} \tag{3.5}$$

where $U_1$, $U_2$, $U_3$, and $U_4$ are the control outputs to the system, $z_d$ is the the desired vertical position, and $F_{hover}$ is the force required to maintain a steady altitude. The proportional gain provides a steady increase in control variables to reduce error and converge the current state towards the desired state while the derivative gain reduces the degree to which the system will overshoot. Proper tuning of both parameters will greatly affect the response of the system and the ability to approach a desired state with a stable convergence. A third integral parameter is typically utilized in the convergence of fully actuated mechanical systems however for our underdamped and underactuated system the addition of an integral term would force the system unstable.

## 3.4 Simulation

The controller was implemented in MATLAB® Simulink to verify trajectory tracking and tune the controller gains. For this initial investigation the controller gains were tuned manually until the system converged. The output of the system tracking a helical trajectory is shown in Figure 3.3. The desired path of this trajectory is defined by the state Equation (3.6) where x position and y position follow a set

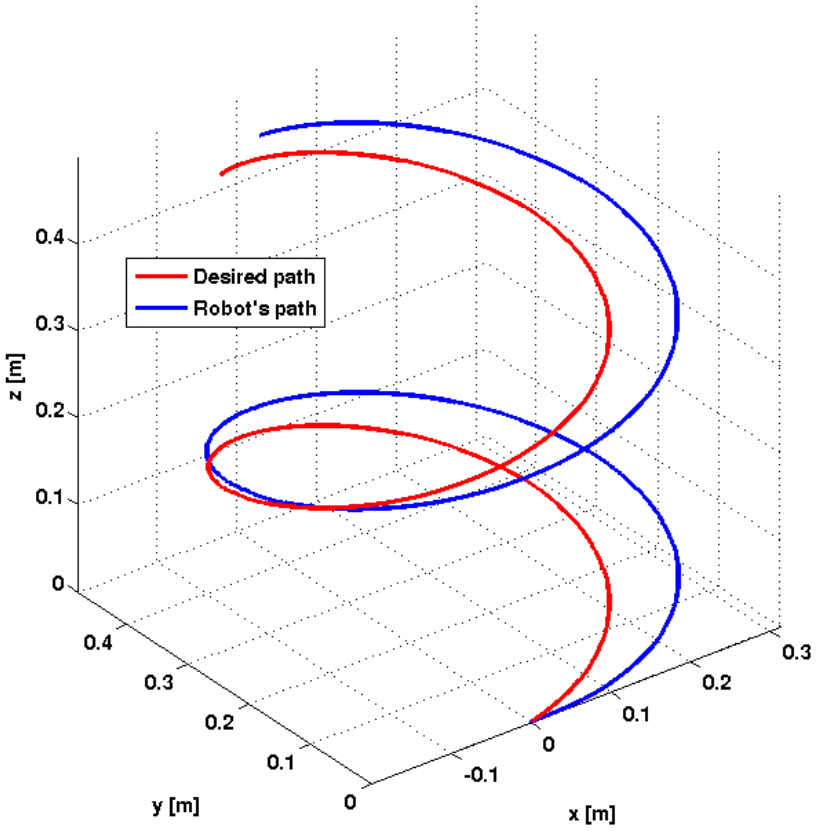


Figure 3.3: Graph of the Desired Trajectory and actual Trajectory of a Simulated 3D Point to Point Relocation.

radius and z position is a function of time. The implemented controller, utilized the simplified dynamics described in Chapter 2

$$\overline{x} = \begin{bmatrix} V_x cos(\psi(t)) \\ V_y sin(\psi(t)) \\ 0.05t \end{bmatrix} \quad \dot{\psi}(t) = 1 \tag{3.6}$$

whereas the simulation followed the full system dynamics and the characterized real system responses. The system successfully follows a desired trajectory defined by position and orientation with minimal error. It is important to note that system

control error is defined as a function of velocity error as opposed to the more common position error. As such the system initially tries to stabilize about hover, before correcting for position error. This initial delay coupled with the control strategy prevents the vehicle from minimizing system position error as is apparent with the presented error in the path following.

## 3.5 Summary

This chapter presents a discussion of the design and implementation of a PD controller for spatial translations. The PD controller was developed based on the previously defined dynamic model of the dual-axis tiltrotor. Use of the simulation described in the previous chapter allowed for the implementation of the controller on a simulated system in order to tune the proportional and derivative gains appropriately. The simulated was used for multiple stages in controller testing and development leading up the the successful track a helical trajectory.

# Chapter 4

# Realization

This chapter presents an in-depth discussion on the mechanical, electrical, and software implementation of the tiltrotor aerial vehicles. The following sections describe the design of the micro (uTRo) and full sized (TRo) aerial vehicles. Addressed in detail are, the design of each prototype system, the system electronic structure, the software program flow, and the implemented methods for calculating attitude and heading of the system.

## 4.1 Full Scale Tiltrotor (TRo) Aerial Vehicle

The TRo aerial vehicle was designed to facilitate autonomous indoor and outdoor flight, capable of high speed aggressive maneuvers. A CAD rendering of the fully assembled vehicle is depicted in Figure 4.1 labeling all of the components used in the construction of the aerial vehicle. An accompanying exploded view of the TRo depicting all of the components used in the system is shown in Figure 4.2. The aerial vehicle is constructed using a rigid body frame that connects two nacelle units located symmetric about the sagittal plane of the body.

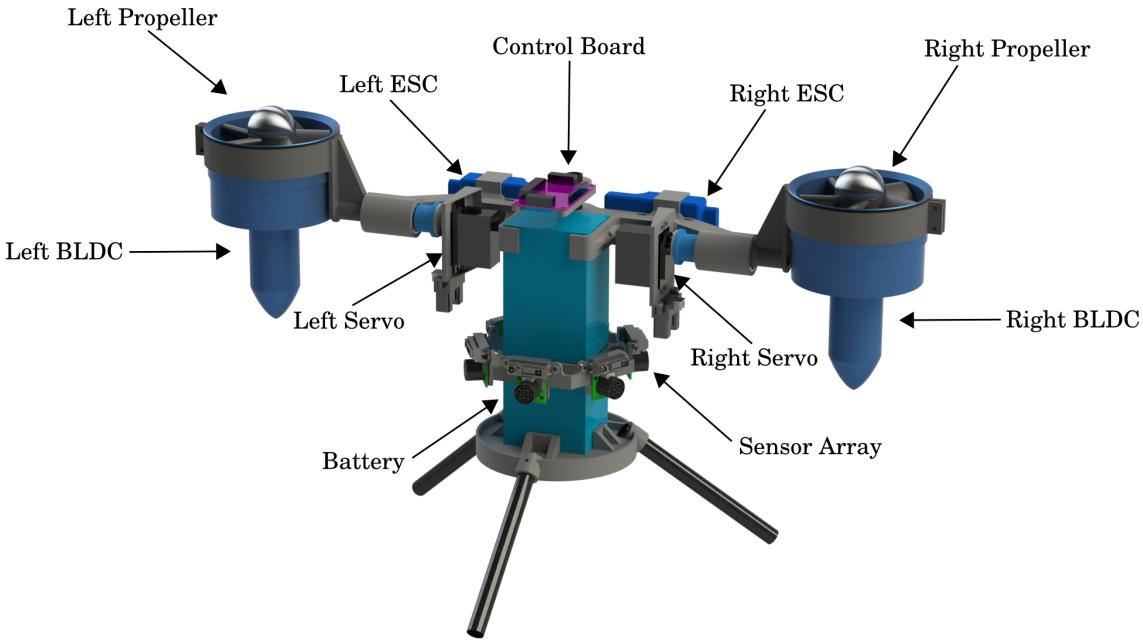


Figure 4.1: A CAD rendering of the TRo aircraft.

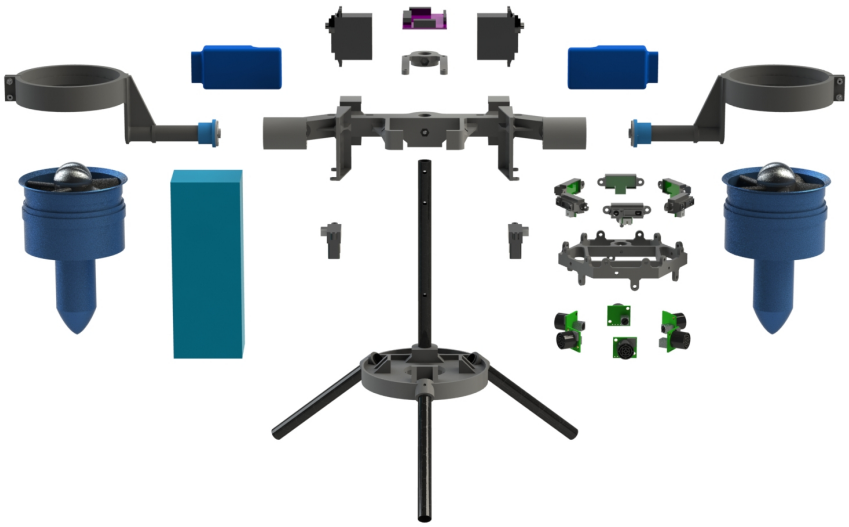

Figure 4.2: Exploded CAD rendering of all components used in the TRo.

### 4.1.1 Hardware Selection

Each of the nacelle units is comprised of a Hitec digital servo, a 3D printed motor mount, and an off-the-shelf five bladed high dynamic thrust ducted fan unit shown

in Figure 4.3. The ducted fan unit is purchased fully assembled and comprises of

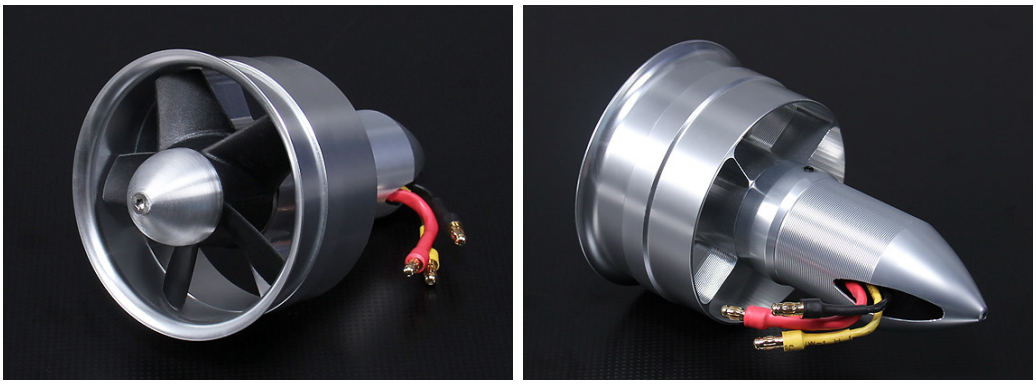

(a) Front view of the ducted fan unit. (b) Side view of the ducted fan unit.

Figure 4.3: Fully assembled ducted fan unit used in the TRo system

a 1900kv 80A brushless in-runner BLDC, an aluminum propeller mount, a fiber-glass reinforced ABS plastic propeller, and a CNC machined aluminum housing. To prevent system yaw rotation as a result of the thrust normal, counter rotating propellers are used on the two motors. A disassembled CAD rendering of the system is shown in Figure 4.4. The following TRo frame components were manufactured

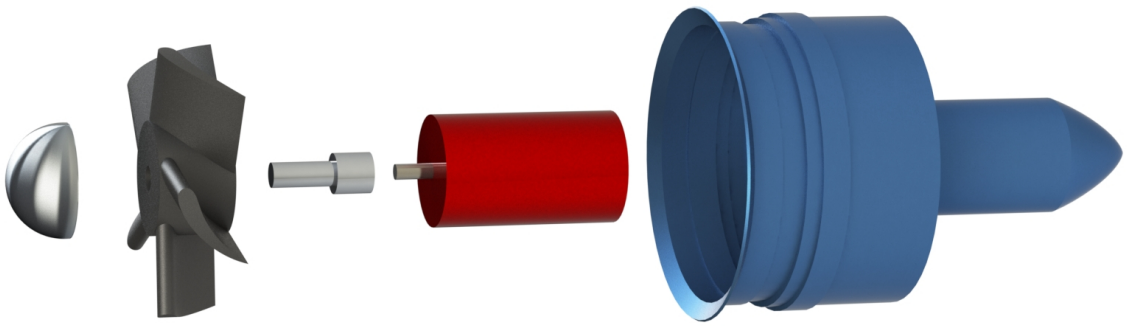

Figure 4.4: A CAD rendering of all components contained within the ducted fan unit.

using a Stratasys Dimension 3D printer: the base support shown in Figure 4.5a,

the sensor bracket shown in Figure 4.5b, the T frame shown in Figure 4.5c and the motor mount support shown in Figure 4.5d.

The 3D printed parts provide an interconnection mechanism for the control board, the proximity sensing components, the brushless motor drivers, the servos, the motor mounts, the motors, and the battery. These components are connected through a backbone comprised of a 0.5in pultruded carbon fiber tubing which is also used as the angled legs to support the entire system. The air frame components were designed to reduce overall system weight without severely impacting strength. This was achieved through the use of a low plastic volume interior honey comb structure. The system is symmetrically designed about the sagittal plane with the battery affixed to the vertical z-axis of the MB. The system exhibits increased stability due to the fact that the C.G. of the system is located below the center of rotation.

The on-board controller is an Ardupilot Mega 2.5 module shown in Figure 4.6. This board is powered by an Atmega 256 embedded microprocessor and is supplemented with a 9 axis IMU, altimeter, and connection points for a wireless telemetry and GPS system. The autopilot hardware is connected to 2 100A ESCs, 6 ultrasonic range sensors, 6 short range infrared sensors, 2 long range infrared sensors, and a 5 cell 10Ah LiPo battery. The fully assembled aircraft weighs 2.8kg while the two ducted fans are rated for a maximum thrust of 3.2kg at 22V and 80A each. The system thrust to weight ratio at maximum power draw is 2.3:1, calculated using Equation 4.1.

$$Duration_{est} = \frac{Power_{Supply}}{Power_{Draw}} \tag{4.1}$$

The vehicle utilizes sensors for autonomous take off and landing, point to point relocation, and obstacle avoidance. Once again the battery placement restricts the center of gravity of the aerial vehicle below the rotational plane of the two nacelle units and within the physical battery itself. Figure 4.7 presents the final realized

(a) The TRo base support structure.

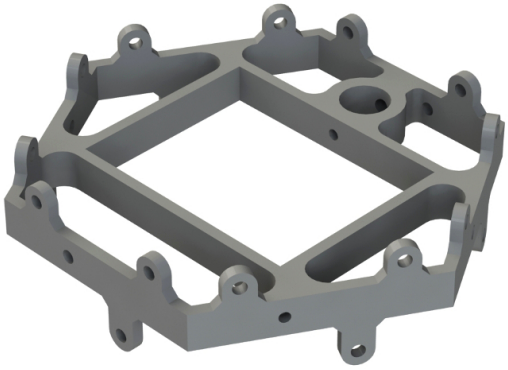

(b) The TRo sensor bracket.

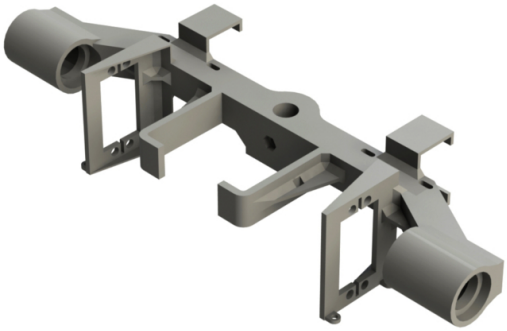

(c) The TRo T frame.

(d) The TRo Motor mount.

Figure 4.5: CAD renderings of 3D printed TRo components.

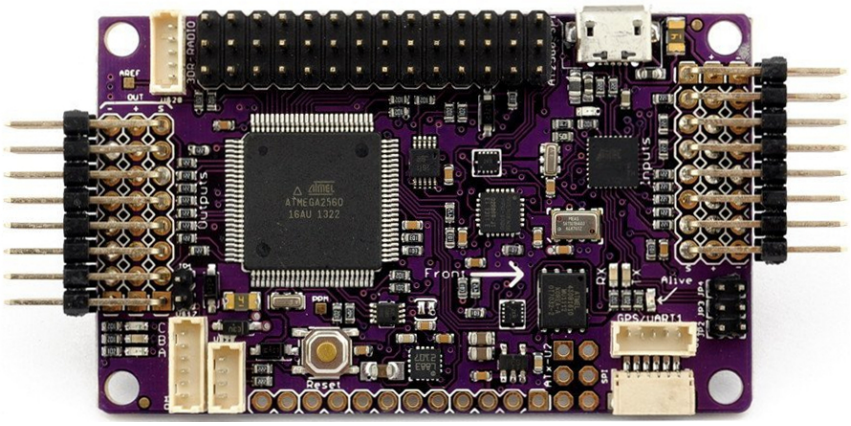


Figure 4.6: TRo main control board.

design of the full scale tiltrotor aerial vehicle.

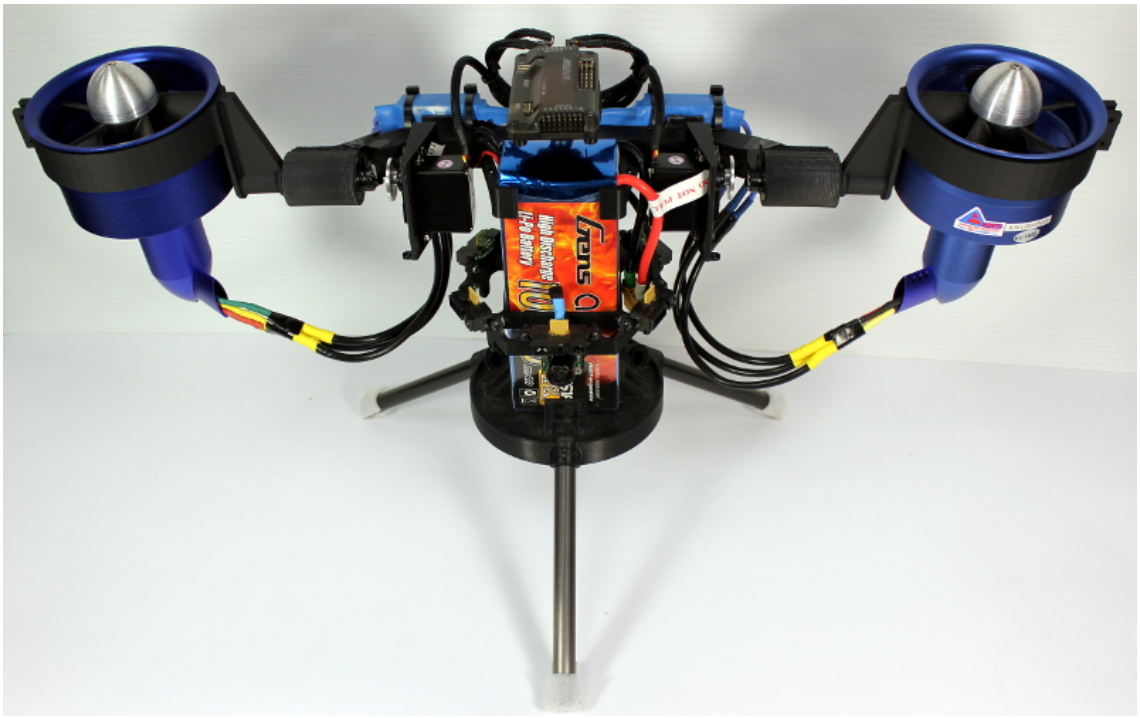

Figure 4.7: The realized full scale tiltrotor.

### 4.1.2 System Layout

Figure 4.8 is a block diagram of the the full scale tiltrotor electrical system. The image is a comprehensive visualization of the components, the connections between them, and their respective communication protocols. The main control board is

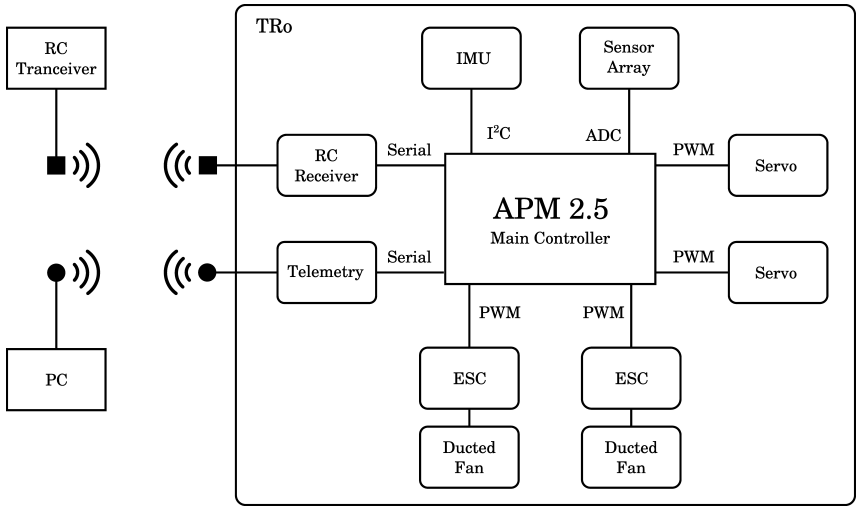


Figure 4.8: The electronics block diagram of the full scale tiltrotor.

the central information hub for the system. Information between the main control board and the external PC is accomplished through the use of a wireless telemetry kit. Similarly control signals from a human operator are sent to the main control board through a wireless RC transceiver and receiver combo. Information about the attitude of the system is continuously gathered from the IMU over an $I^2C$ communication bus. Information pertaining to local obstacles is calculated through the use of an analog to digital converter. Finally connections to the system actuators are completed using a pulse width modulated signal ranging from 600 to 2400 $\mu$sec.

### 4.1.3 Software

In choosing the APM 2.5 autopilot hardware, a large array of open source software libraries were pre-written for the components on board. As such far fewer embedded software libraries needed to be written. Figure 4.9 is a flowchart depicting the high level software initialization and control sequence for the embedded microprocessor. Upon start-up the system begins an initialization sequence to determine the orientation of the control board relative to the world coordinate frame. Once the attitude, heading, and reference system (AHRS) has initialized the aerial vehicle transitions to the main control loop, run on board the embedded microprocessor, and is armed for flight. Run at 50Hz, the main control loop begins by sampling for RC trajectory inputs either from a human pilot, or telemetry signals from a computer. The system continues to cycle through the next 6 steps regardless of a trigger input. A request is sent to the IMU for data to update the AHRS system. Once the AHRS) is updated new control signals are calculated to maintain stable flight. The control signals are converted to output PWM signals and sent to the respective motor controllers to adjust propeller thrust or nacelle angle. Finally the system completes the loop by sending a list of updated parameters including a heartbeat message to the PC ground station for new way point calculations.

## 4.2 Micro Scale Tiltrotor ($\mu$TRo)

The micro scale tiltrotor, $\mu$TRo, was designed as a low cost, low power, easily assembled, and robust test platform for indoor use. The system is smaller, requires less power, produces less thrust, and is inherently more safe. The main consideration for the design of the $\mu$TRo was weight. A CAD rendering of the $\mu$TRo is shown in Figure 4.10 labeling all of the components used in the construction of the aerial

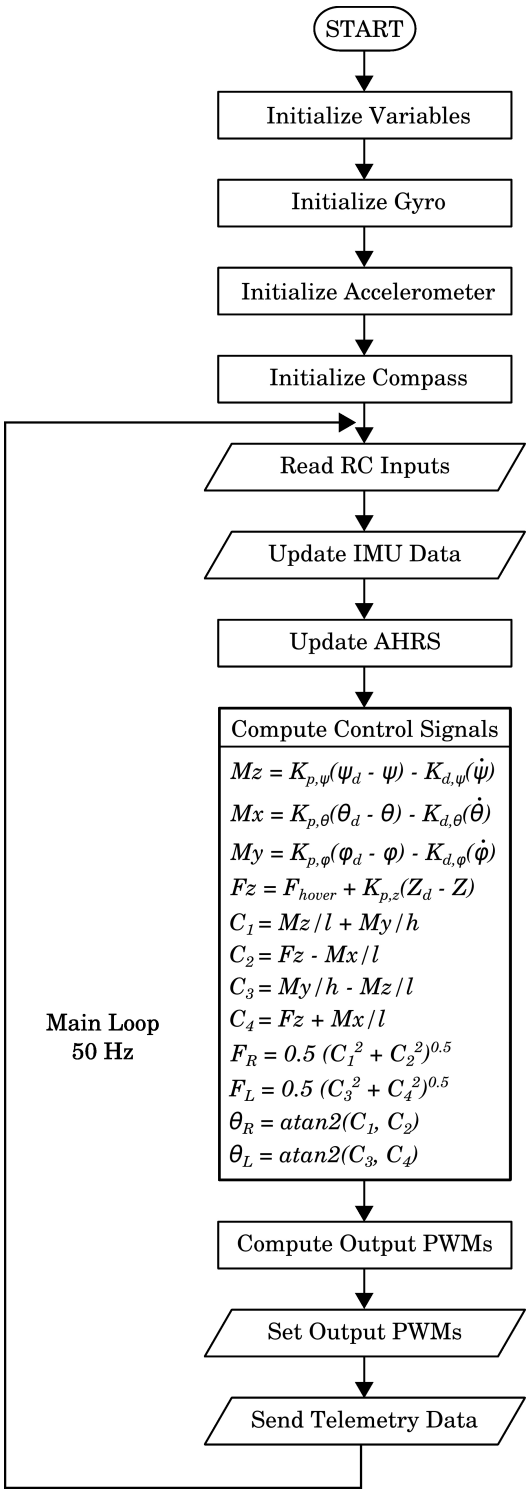


Figure 4.9: The full scale tiltrotor software flow chart.

vehicle. A picture of the disassembled $\mu$TRodisplaying the individual components

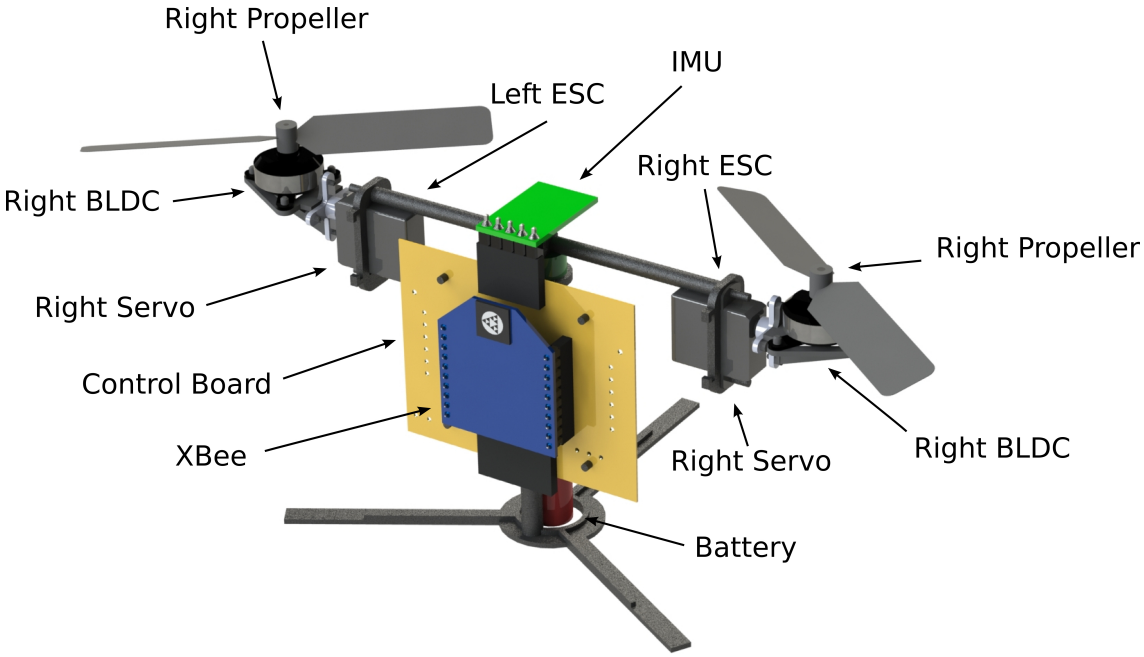


Figure 4.10: A CAD rendering of the $\mu$TRo aircraft.

used in the construction of the aerial vehicle is shown in Figure 4.11.

### 4.2.1 Hardware Selection

Like the TRo, the $\mu$TRo is propelled using two symmetrical nacelle units. Each of these units is comprised of a micro servo providing pitch rotation, a specialized servo horn, a 7,000kv 3A brushless out-runner DC motor (BLDC), and a 3in propeller with a 2in pitch. To reduce the weight of the system, the servo horn was used as a mounting bracket for the BLDC and subsequent propeller unit. To prevent system yaw rotation as a result of the thrust normal, counter rotating propellers are used on the two motors. The vehicle body and specialized servo horns, shown in Figure 4.12, are constructed using an additive fused deposition manufacturing process forming single continuous structures.

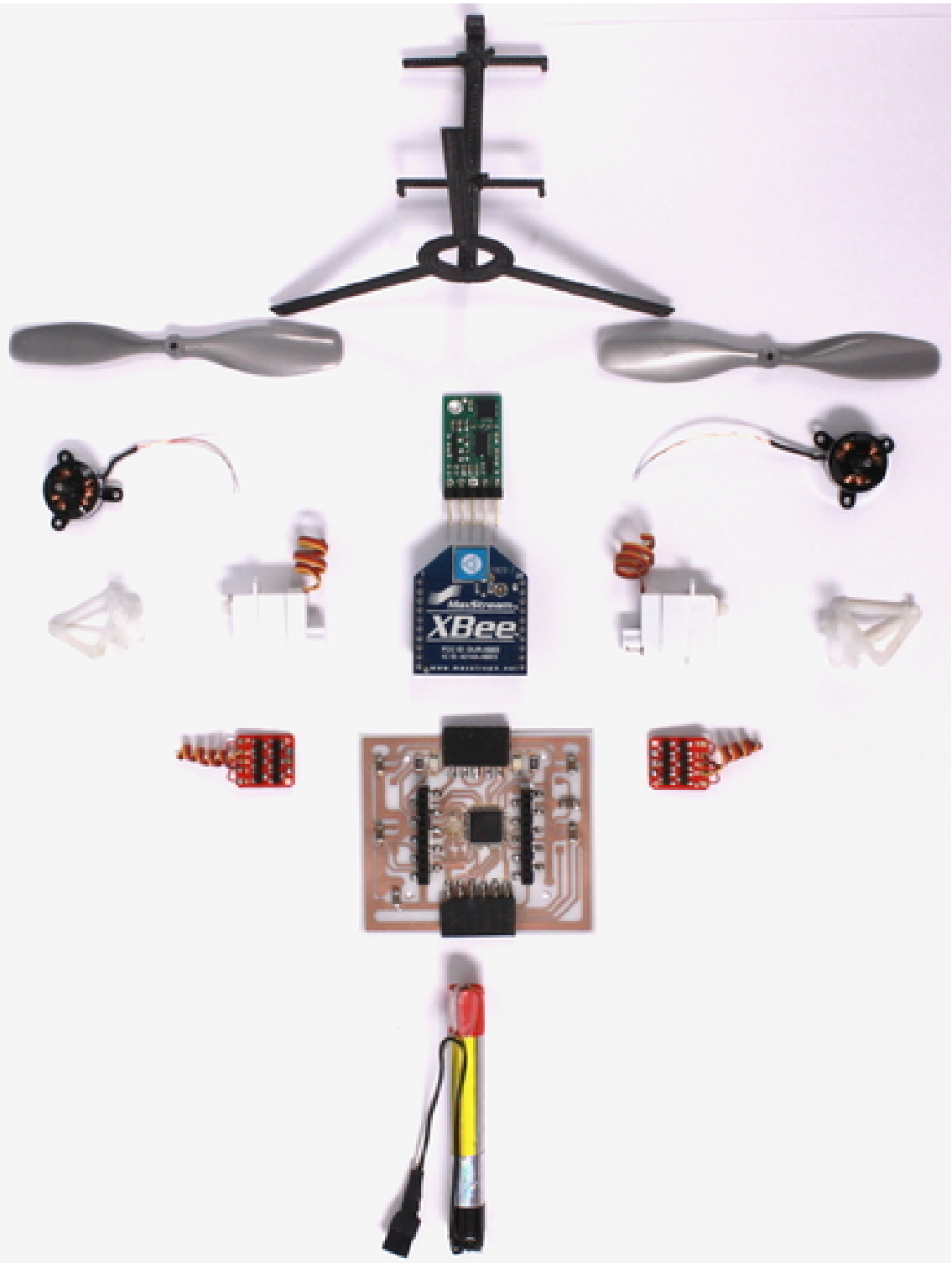


Figure 4.11: A disassembled view of all components used in the $\mu$TRo.

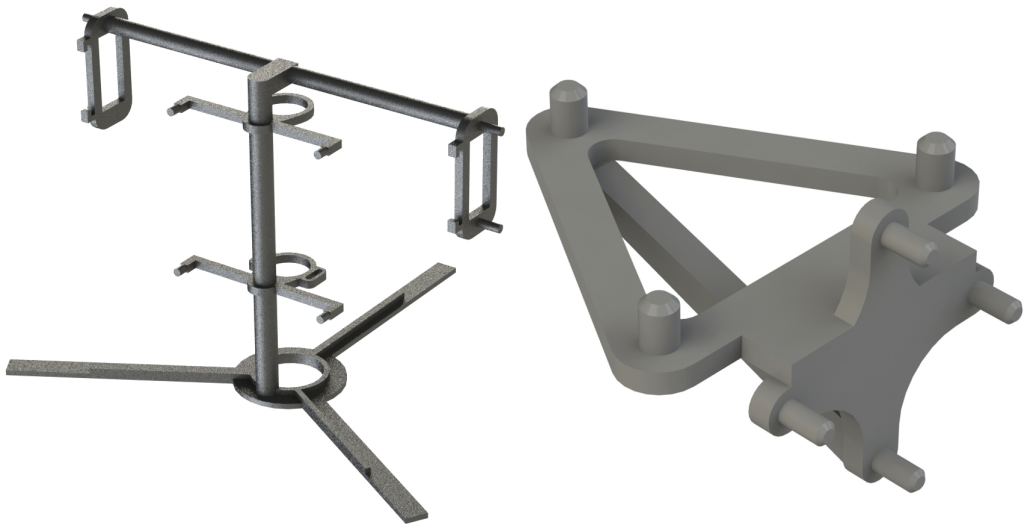

(a) $\mu$TRo body frame. (b) $\mu$TRo servo horn.

Figure 4.12: CAD renderings of the 3D printed $\mu$TRo components

Two methods of printing were used in the construction of the $\mu$TRo: 3D printed ABS plastic for the MB frame and PolyJet Digital material for the servo horns. The air frame structure is optimized for reduced weight, incorporating fastenerless rigid mounting locations for all on-board electronics, servos, and brushless DC motors. The component locations were placed symmetrically about the sagittal plane and the battery was placed along the z-axis of the craft. The design restricts the C.G. of the craft to a location within the body, specifically, within the battery itself. This calculated distribution of weight lowers the C.G. of the aircraft below the center of rotation improving the stability of the system.

The $\mu$TRo is controlled with an Atmega 88p embedded microprocessor mounted on top of a custom acid etched printed circuit board (PCB), shown in Figure 4.13. The circuit provides connections to the following peripherals: a Xbee wireless transceiver, two micro servo motors, two 3A brushless DC motor drivers (ESC), a 9 axis IMU unit, and a single cell 270mAh LiPo battery. The completely assembled system weighs 30g with each brushless DC motor producing a maximum of

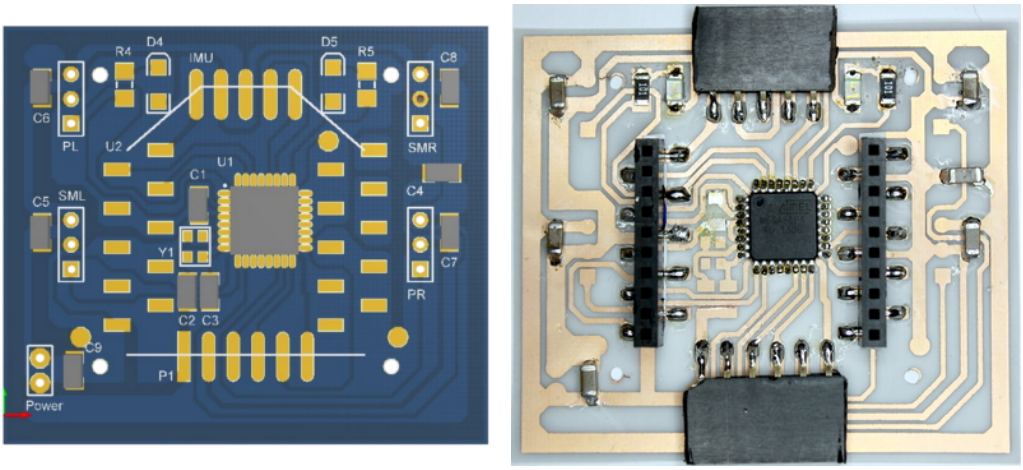


(a) CAD drawing of the Designed PCB. (b) Photograph of the etched PCB.

Figure 4.13: The designed and printed PCB board for the $\mu$TRo aerial vehicle.

26g of thrust at 4v. The summation of both maximum motor forces with respect to the weight of the aircraft gives the system a thrust to weight ratio of 1.6:1. To determine the maximum flight duration of the $\mu$TRo, the following assumptions were made: negligible current draw due to communication, computation, and sensor polling with an assumed ideal operation of the system. Based on the given assumptions, the maximum flight duration, calculated using Equation 4.1, is 2.7 minutes at maximum thrust and 5.9 minuets at hover. The final realized system is shown in Figure 4.14.

### 4.2.2 System Layout

Figure 4.15 is a block diagram of the micro scale tiltrotor electrical system. Similar to the full scale tiltrotor electronics block diagram this image presents a visualization of the micro scale electronics system. Once again the main control board is the center of focus connecting all of the component peripherals together. Trajectory updates exchanged between the external PC and the microprocessor is communicated


Figure 4.14: The realized micro scale tiltrotor.

wirelessly through an Xbee communication module. Current attitude and heading readings are continuously gathered from the IMU over an $I^2C$ communication bus. Finally connections between the controller and actuatable peripherals are sent using a pulse width modulated signal ranging from 600 to 2400 $\mu$sec.

### 4.2.3 Software

Figure 4.16 is the high-level software flowchart for the micro tiltrotor aerial vehicle. The routine is responsible for initializing all of the global variables, the AHRS system, the timers, interrupt service routines (ISRs), and begins a visual heartbeat communication using an LED. The software instantiates multiple loops that define actuator command messages, sensor sampling rates, and communication protocols.

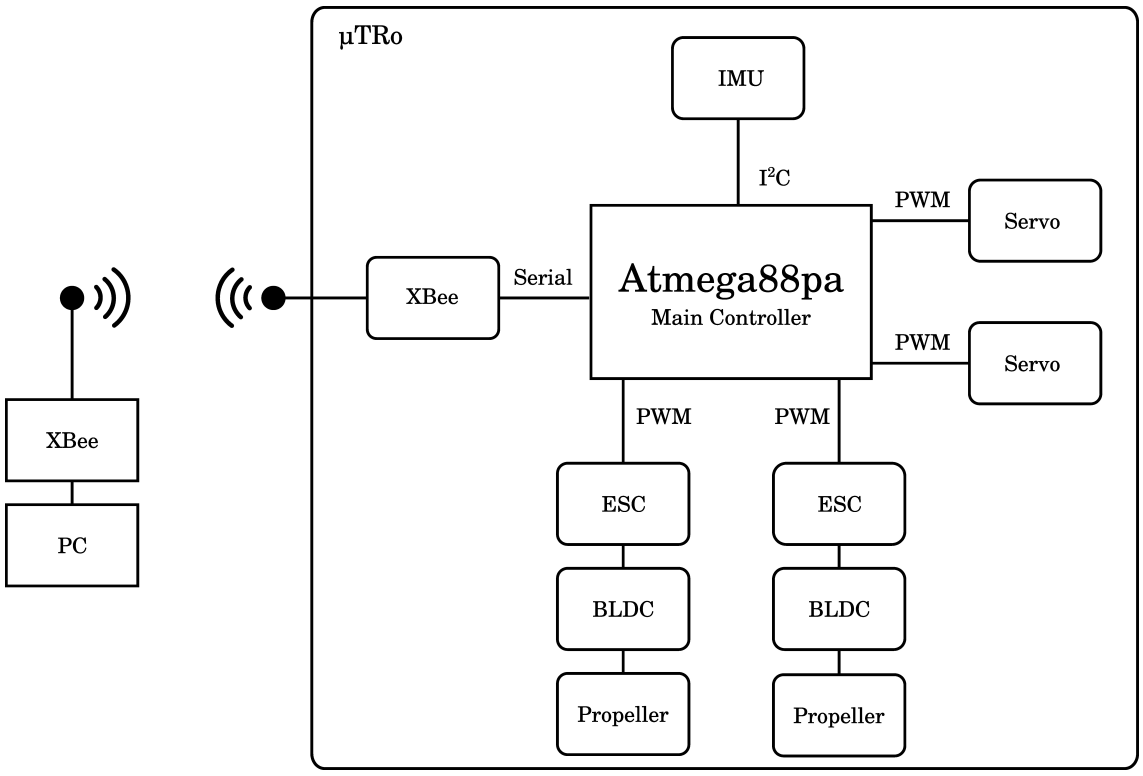


Figure 4.15: The electronics block diagram of the micro scale tiltrotor.

Once the control loop has finished initializing the timers it proceeds to establish the USART protocol. Figure 4.17a presents the USART interrupt service routine for the micro scale tiltrotor. The USART ISR is responsible for communication back to the external PC. The routine initially checks for available data either returning to the main program flow if there is nothing to be read, or gathering the data if there is information in the buffer. Once the data is collected the information is parsed as either as a command sequence or discarded as an incomplete command flushing the buffer. After gathering the information the software progresses to the high speed control loop. Figure 4.17b presents the 100Hz interrupt switching routine for the control loop. The 100Hz ISR is comprised of an oscillating routine producing two separate 50Hz loops. These loops are divided into a pulse position modulation (PPM) command loop, and a system control loop. The system control loop parses

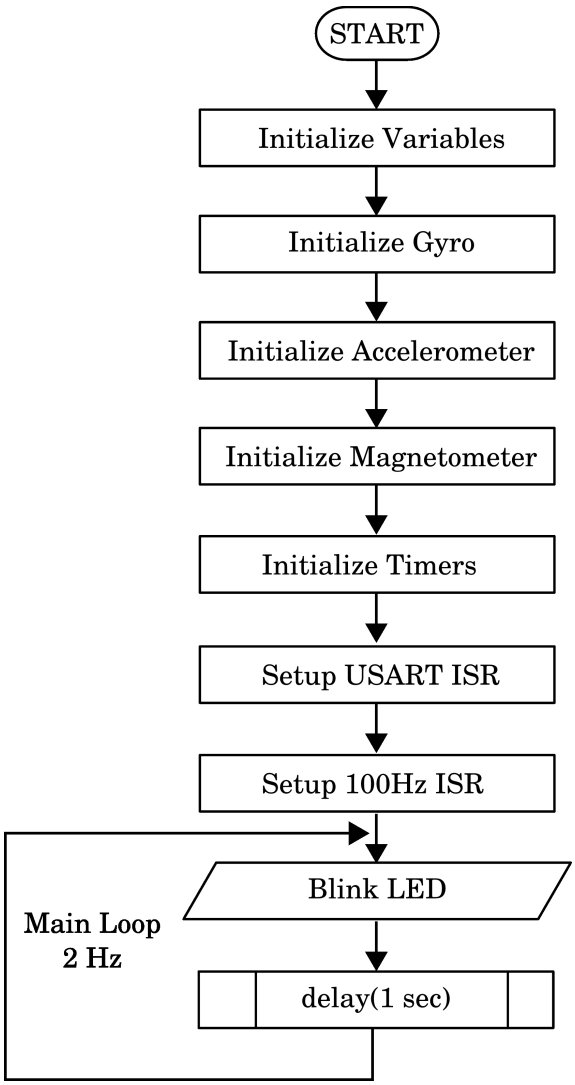


Figure 4.16: The micro scale tiltrotor software flowchart.

the polled IMU data, updates the AHRS and utilizing the onboard control laws, computes the next iteration of control outputs. Figure 4.18a depicts the embedded controller flowchart for the micro tiltrotor. The output PWM values are determined and passed into a buffer for the next 100Hz control iteration which are subsequently passed to the PPM routine. Figure 4.18b presents the pulse position modulation routine.

The PPM routine instantiates all PWM pins to a low value, assigns a count

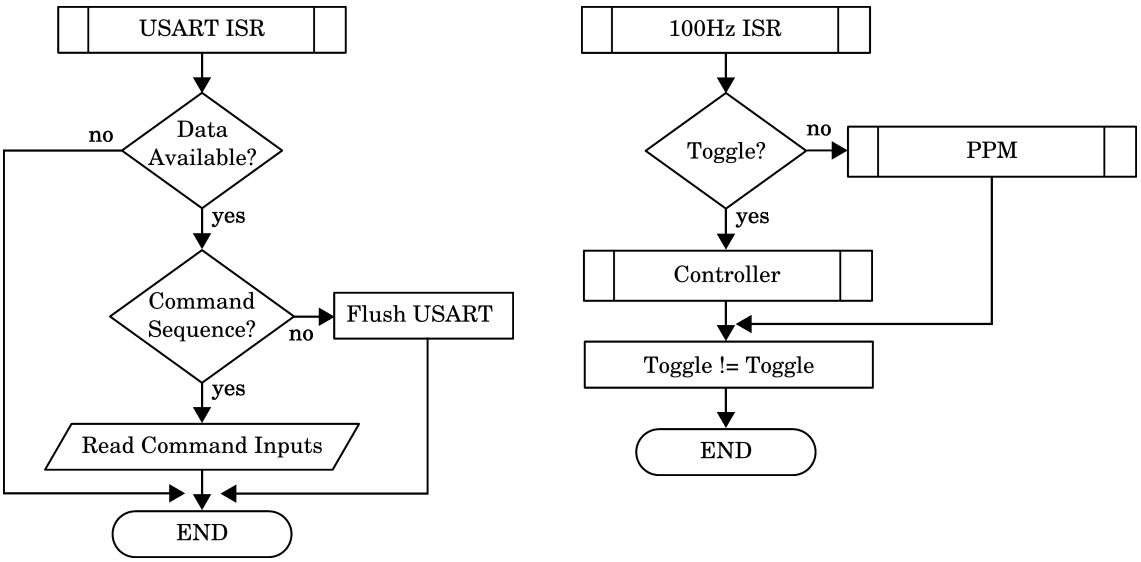


(a) USART ISR. (b) 100Hz ISR.

Figure 4.17: The micro scale tiltrotor ISR flowcharts.

and triggers the appropriate PWM output based on the duty width and output pin for each of the 4 motors. Figure 4.19 is a visual representation of the modified PPM software, implemented for the control of all 4 motors.

## 4.3 Attitude Heading and Reference System (AHRS)

Aerial vehicles are described using 6 DoF, therefore they require a minimum array of sensors monitoring the body coordinate frame with respect to the world coordinate frame, to correctly observe and define the current system state. As with any autonomous system, sensory information gathered about the current state is used by the system control equations to minimize error. The AHRS is a typical method for measuring the three axes of rotation that provide the heading, attitude, and yaw information of the aircraft, essential for autonomous localization, with respect to the world coordinate frame. Typical methods utilize the sensor fusion of either

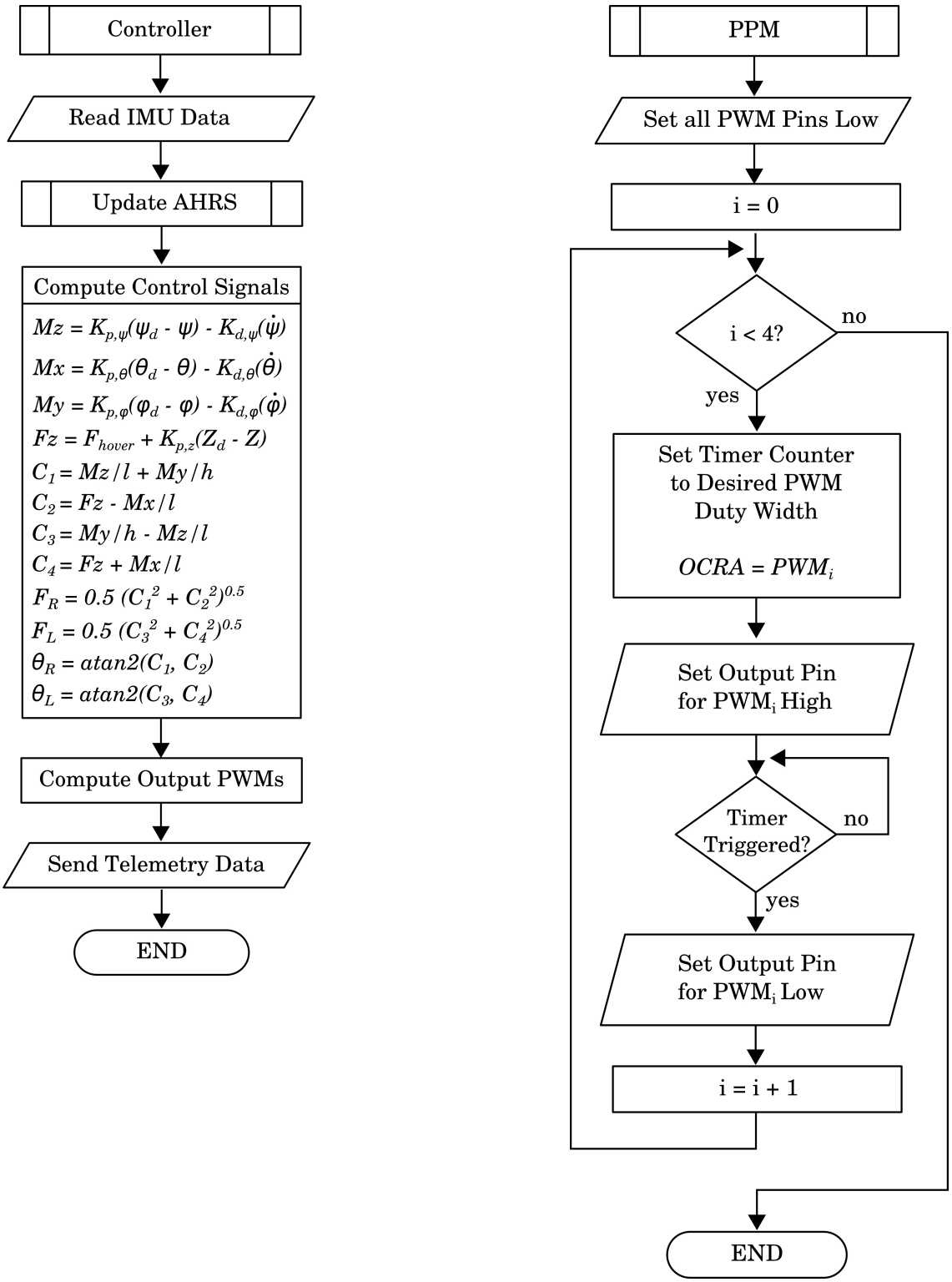


(a) Micro scale tiltrotor controller.

(b) Micro scale tiltrotor pulse position modulation.

Figure 4.18: The micro scale tiltrotor software routine flowcharts.

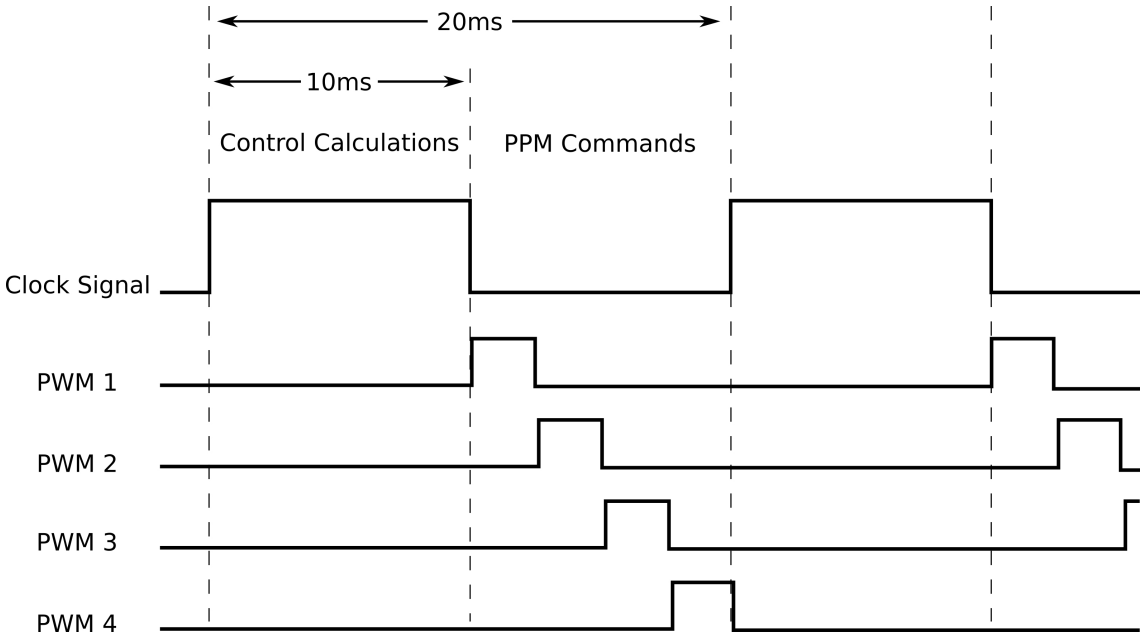


Figure 4.19: The micro scale tiltrotor PPM signal example.

solid state or microelectromechanical systems such as gyroscopes, accelerometers and magnetometers on the three body axes to ascertain changes in system pose and in some cases, interpolate system position. This information is most commonly derived into Euler angles describing the system orientation with respect to the body fixed frame. Multiple methods are used to filter and converge this information to a body rotation giving the aerial vehicle a pose and heading with respect to the world coordinate frame. In the case of this project two implementations were pursued: Sebastian Madgwick's gradient descent approach [25] and Robert Mahony's DCM Filter [26]. These methods are used to contribute roll pitch and yaw information with respect to the world coordinate frame and along with GPS and altimeter sensors, the system is fully observable. The two methods implemented were optimized for the fastest convergence possible to reduce sensor noise and increase system accuracy. Madgwick's software approach utilizes an efficient orientation filter for inertial and magnetic sensor arrays. The filter implements quaternion representation,

removing Euler angle gimbal lock. However, the quaternion representation allows for infinite solutions, thus accelerometer and magnetometer data is used in an analytically derived gradient-descent algorithm to compute gyroscope measurement error. Mahony's DCM filter approaches the same AHRS problem as deterministic observer kinematics posed on the special orthogonal group $SO(3)$ driven through reconstructed attitude and angular velocity measurements.

## 4.4 Discussion

Initial design constraints on the aircraft included a 15 minute flight time, the ability to autonomously navigate both indoors and outdoors, vertical take off and landing, and agile flight. Off-the-shelf components were chosen when available to reduce redundant system design, increase manufacturability, and shorten the time to produce a functional prototype. Ducted fans were chosen for the full scale tiltrotor vehicle due to their inherent safety, high thrust at high motor speeds, and low propeller inertia. The ducted fan shroud has multiple purposes in this design, not only does it help produce increased thrust by accelerating airflow over the airfoil surface but it also provides a rigid structure to protect both the motor and propeller from damage in minor collisions. The ducted fans are known to produce higher thrust than open air propellers of similar size because the outer housing helps prevent airflow delamination at higher RPMs, causing cavitation and subsequently a loss of thrust. Unfortunately at the design and realization of this project, high static thrust ducted fans were unavailable for purchase in the desired size, however, it is a strong recommendation for future work, due to their higher thrust output at static airspeed effectively promoting more efficient hover. Limited component availability was the largest driving factor in the design of micro scale tiltrotor; most of the components

used in the full scale tiltrotor are unavailable in a smaller form factor. As size decreases, typically, power density, power efficiency, and component quality decrease, for a similar price point.

## 4.5 Summary

In summary two tiltrotor vehicles were realized. An in depth discussion of the design process was outlined for the choice of hardware components, system electrical layout, and software subsystems. The discussion and implementation of two different methods for AHRS system convergence were presented. The choices in physical components were evaluated by: availability, ease of integration, robustness, and cost.

# Chapter 5

# Analysis and Experimental Results

This chapter presents the component analysis and experimental demonstrations conducted on the $\mu$TRo and TRo aerial vehicles. The first section describes the experimental study on the performance of the $\mu$TRopropellers and the TRo ducted fans. The second section describes the experimental study and analysis on the IMU readings from both aerial vehicles. The final section presents the experimental demonstration of both aerial vehicles in hovering, and altitude and yaw maneuvering while tethered and remotely controlled.

## 5.1 Propeller and Ducted Fan Performance

For thrust generation, the $\mu$TRo utilizes counter rotating propellers while the TRo utilizes high-speed ducted fans. To successfully control the system in flight, the correlation between output thrust and the input signal (PWM width) must be calibrated. However, due to the variability in manufacturing and the necessary precision

for controlled flight, the correlation between output thrust and input signal must be determined experimentally under expected running conditions. The following sections describe the experimental setup and results of the propeller and ducted fan control calibration. During the experiment, the supply voltage and current draw of the propellers and ducted fan units were also recorded to determine power consumption at varying speeds.

### 5.1.1 Experimental Setup

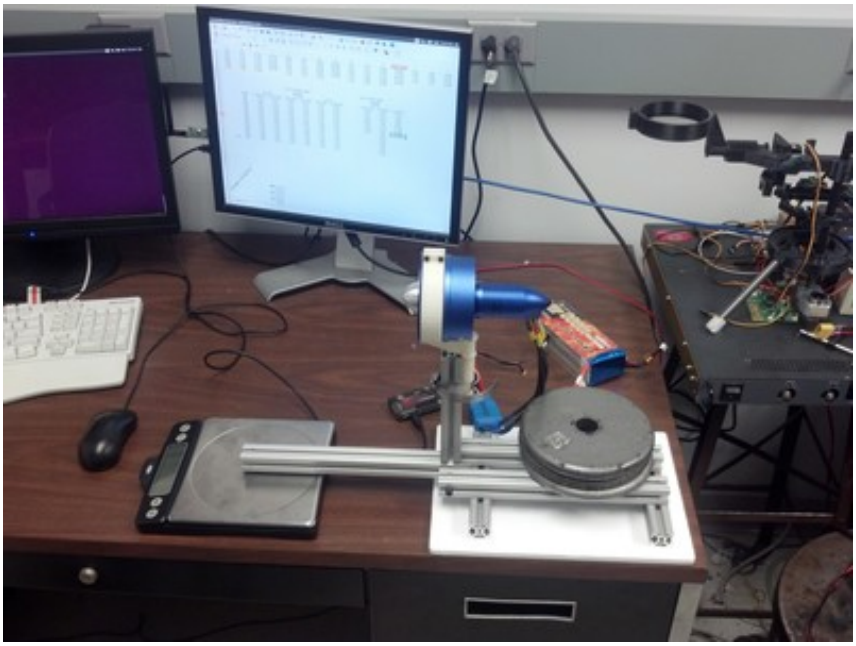

Figure 5.1: The experimental test setup for evaluating the performance of the propellers and ducted fan units.

Figure 5.1 shows the experimental test setup for evaluating the performance of the propellers and ducted fan units, and the consistency of the brushless motor controllers. The experimental setup consisted of a L-angle rig with a propeller or ducted fan rigidly attached to it, a scale to measure the thrust generated by the propeller or ducted fan, a microcontroller to generate the desired PWM signal, a

power supply with a voltage and current readout, an 18.4V 5S 50C 10Ah LiPo battery and a computer connected to the microcontroller to set the desired PWM output signal and to record the measured values.

The experiments were carried out by sweeping through the PWM pulse width, starting at the minimum value that initiated turning of the propeller or ducted fan, and increasing the PWM pulse width at increments of 50 microseconds until either a negligible difference of thrust output was measured, or the maximum permissible current draw was reached. At each PWM pulse width step, the thrust, voltage, and current readings were recorded. The experiments were completed with three ducted fans of the same type, two brushless motor controllers for the ducted fans, and two types of propeller. Due to the L shape of the rig, the measured thrust values had to be converted to actual thrust values based on the moments about the hinge of the experimental setup. The measured to actual thrust ratio was 10.375:9.75 indicating that the actual thrust is approximate 94% of the measured thrust.

### 5.1.2 Experimental Results

The following sections present the experimental results of the propeller, ducted fan, and motor controller testing.

#### Propeller Performance

Figure 5.2 presents the thrust comparison between the two propellers tested for the micro tiltrotor aerial vehicle. With the exception of one data point the gray propeller outperformed the black propeller for the tested PWM signals with an average increase in thrust of 1 gram. At max velocity the gray propeller outperformed the black propeller by 1.4 grams of thrust. This difference in thrust results in a 6 %

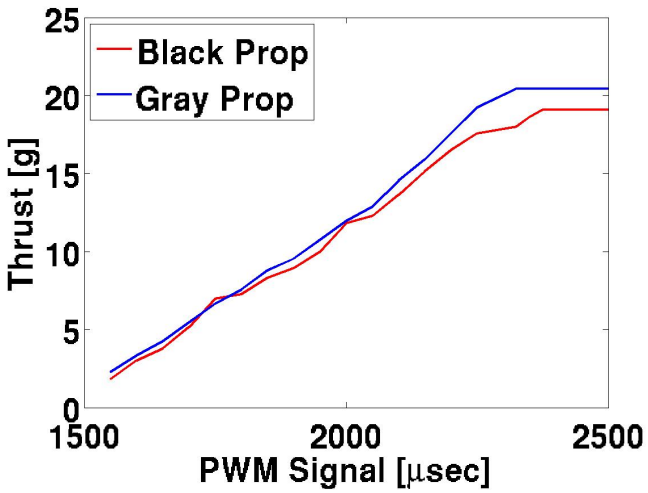


Figure 5.2: The micro tiltrotor propeller thrust data.

change in maximum thrust per motor and a 10 % change in thrust to weight for the entire system.

### Ducted Fan Performance

Four separate ducted fan units of the same type were tested: one counter rotating (CCW) and three regular rotating fans (CW). The ducted fans were labeled as Z (CCW), H (CW), P (CW), and A (CW).

Figure 5.3 shows the output thrust of the ducted fan units versus the input PWM signal. All four ducted fans were tested at 18V (power supply) and 20.67V (LiPo battery), and unit was tested at 22V (power supply). From 5.3, the thrust output versus PWM signal demonstrate a linear relationship. As the voltage is increased from 18V to 20.67V, the slope of the curve is increased. The maximum attainable output at 18V, due to current limiting of the power supply, is approximately 1kg at a 1450 microsecond PWM signal. The 20.67V output has a larger range of operation due to the higher voltage and higher current supply available from the LiPo battery. The maximum thrust output at 20.67V is approximately

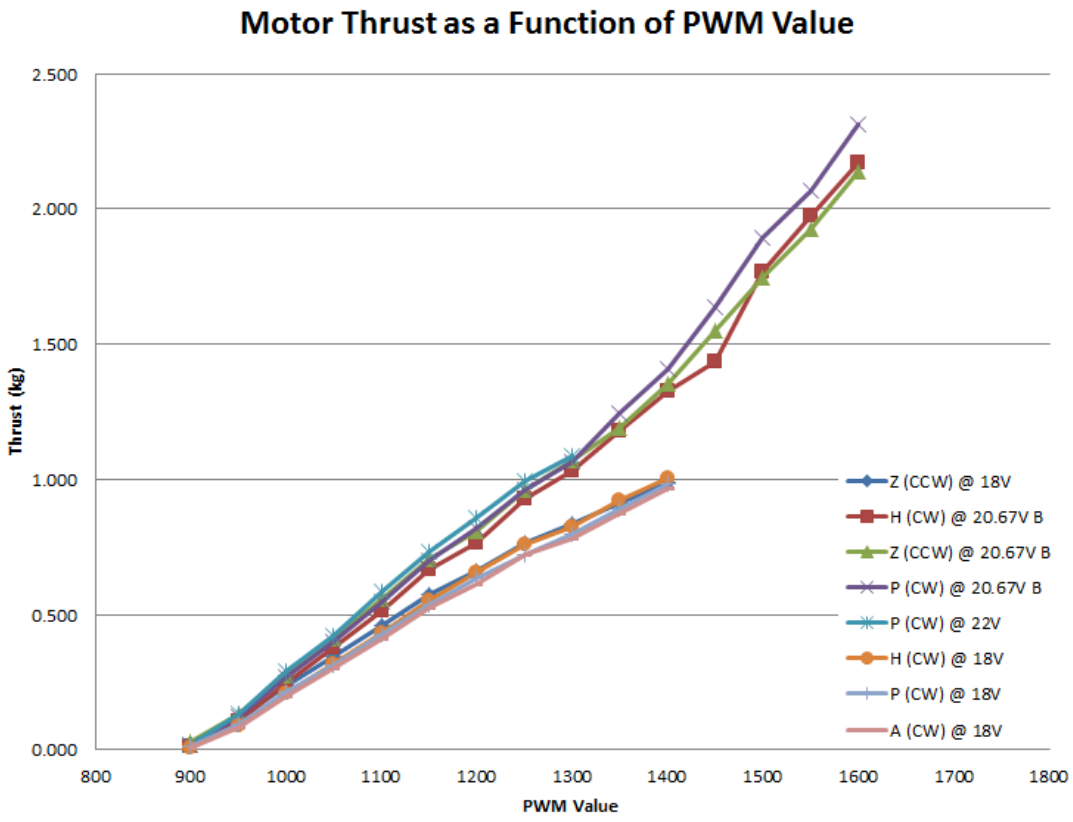


Figure 5.3: Ducted fan thrust characterization data.

2.25kg at a 1600 microsecond PWM pulse width. The ducted fan units showed slightly more variation with the higher voltage. However, the variations are mainly due to the thrust output measurement error, since the thrust reading was performed visually and the readout on the scale would vary approximately 150g and a visual average of the data was recorded. The 22V results do not indicate a significant difference compared to the 20.67V results. Utilizing the thrust versus PWM results, a curve fitting was completed to determine the necessary PWM signal for a desired thrust output.

Figure 5.4 shows the thrust output of the H (CW) ducted fan at two different voltages versus the input electrical power. As expected, Figure 5.4 indicates that

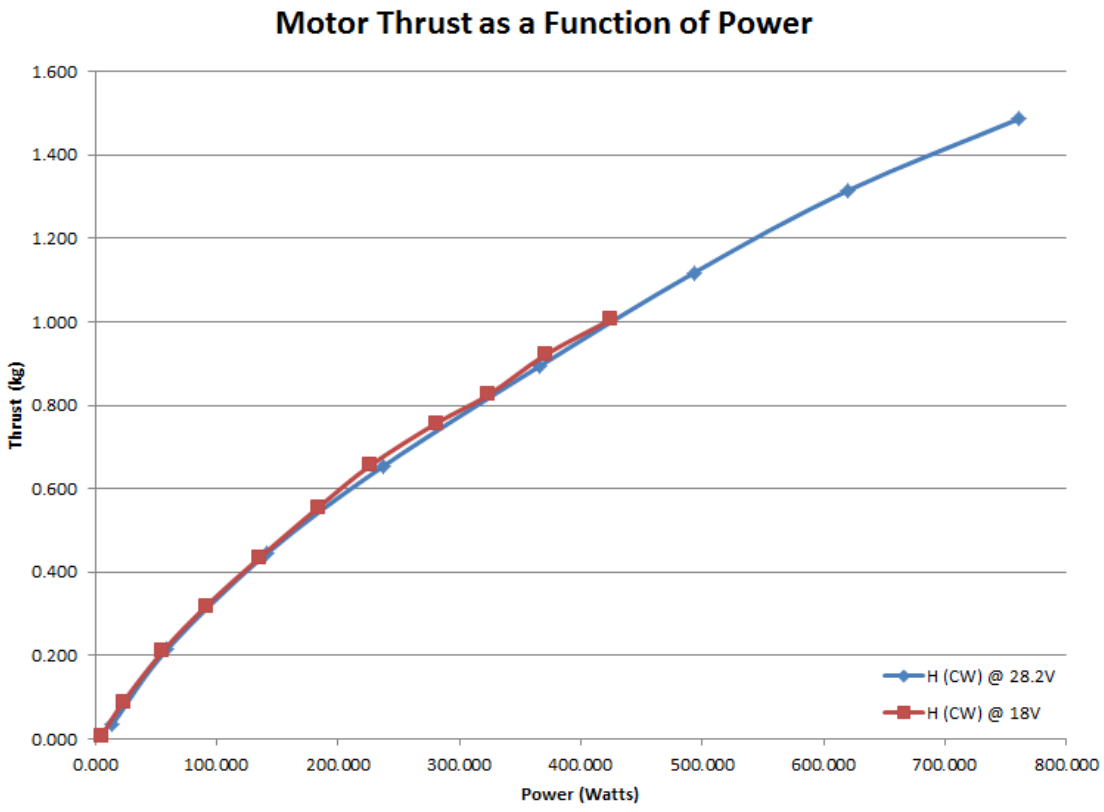


Figure 5.4: Ducted fan thrust versus power input curve.

the motor has the same thrust versus power characteristics at different voltages and that the power consumption increases as the motor velocity and thrust increase. Consequently, Figure 5.4 also suggests that operating the motor at the rated 28.2V results in greater resolution in motor speed through PWM as well as greater overall thrust due to higher power and consequently motor speed at each PWM division.

### Ducted Fan Brushless Motor Controller Consistency

To guarantee output thrust was consistent for both ESC brushless motor controllers, each circuit was connected to the same ducted fan and the thrust versus input signal was measured along with the voltage and current. Figure 5.5 show the output

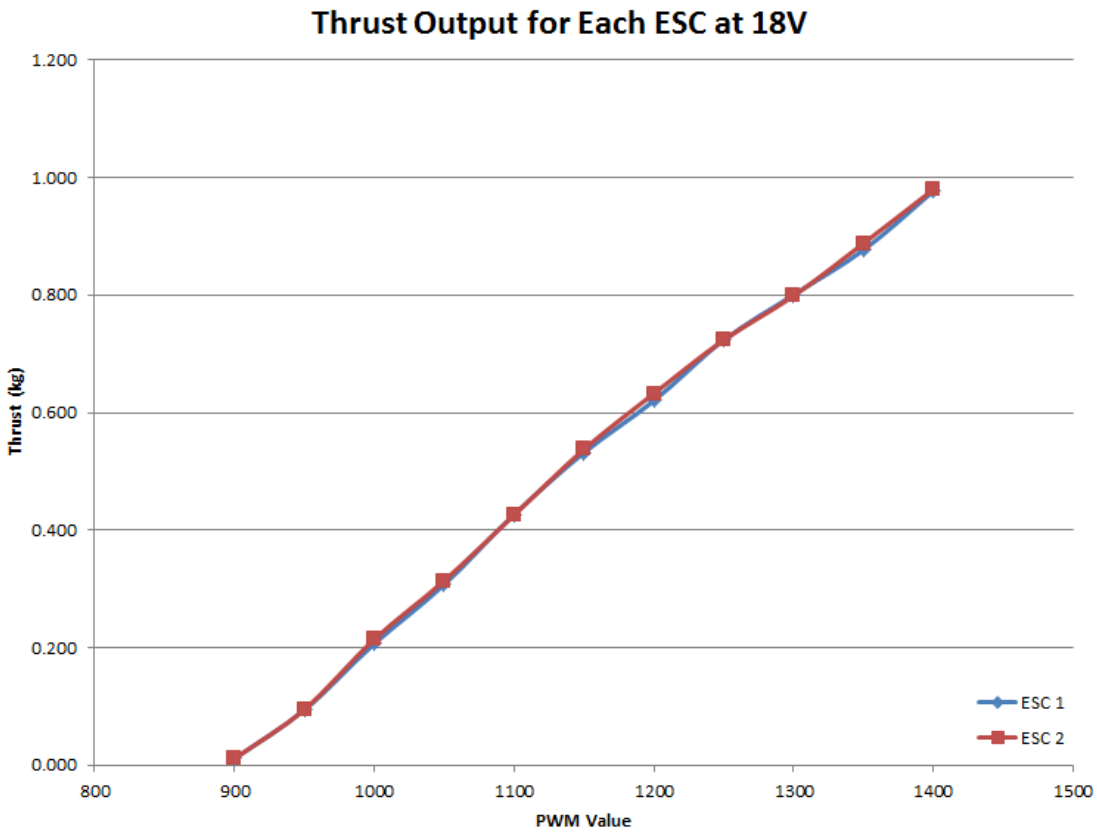


Figure 5.5: The measured output thrust for each 80A ESC using the same ducted fan.

of both ESC brushless motor controllers. From Figure 5.5, the brushless motor controllers exhibit consistent output thrust for a given input signal. Hence, no specific calibration for each individual motor controller is necessary.

### 5.1.3 Discussion

Since all of the the ducted fan units exhibited consistent results, there was no need for generating individual calibration equations. Using the gathered data, a power curve was fitted to the thrust versus PWM results to obtain a function for determining the required PWM signal for a desired thrust output. The power input versus

thrust output of the ducted fan units followed the expected curve and indicated an advantage on extended PWM range and higher thrust resolution at higher input voltages. The ESC brushless motor drivers showed no variation regarding output thrust to input signal. Hence, no individual calibration for each ESC was required.

## 5.2 IMU Performance

The accuracy of the real-time measured tiltrotor orientation and heading is highly dependent on the quality of the acquired IMU data and how it is processed by the AHRS. The IMU output is expected to be noisy due to the rotation of the propellers and ducted fans along with the structure vibration modes. The following sections describe the experimental setup and results of measuring IMU data on the $\mu$TRo and TRo with the propellers or ducted fans turned on and at high speed compared to a control value, with no motor disturbance.

### 5.2.1 Experimental Setup

The experimental setup included the tiltrotor prototype and a computer. For the general case, a program was written and compiled for each tiltrotor controller that sampled IMU data at 50Hz and sent the data to the computer over serial. The computer collected 20 seconds of IMU data using a MATLAB® script.

### 5.2.2 Experimental Results

The following sections present the IMU data acquired over during each test, with and without the propellers or ducted fans rotating at high speed.

Table 5.1: The RMS of the $\mu$TRoIMU measurements with the propellers at full rotational speed.

| | $a_x$ | $a_y$ | $a_z$ | $m_x$ | $m_y$ | $m_z$ | $g_x$ | $g_y$ | $g_z$ |
|---|---|---|---|---|---|---|---|---|---|
| Speed | | $[\frac{m}{s^2}]$ | | | $[Gauss]$ | | | $[\frac{rad}{s}]$ | |
| off | 0.005 | 0.006 | 0.004 | 0.028 | 0.055 | 0.028 | 0.002 | 0.002 | 0.002 |
| full | 0.507 | 0.560 | 0.321 | 0.365 | 2.530 | 1.072 | 0.004 | 0.004 | 0.004 |

### $\mu$TRo IMU data

Figures 5.6a and 5.6b show plots of the accelerometer data acquired at 50Hz with the propellers of the $\mu$TRo at zero and full rotational speed, respectively. With the propellers off, the root mean square (RMS) of the acceleration data for the x-, y-, and z-axis are 0.005, 0.006, and 0.004, respectively. The RMS values of the measured IMU data are listed in Table 5.1. From Figure 5.6b, the noise due to the rotational speed of the propellers completely overwhelms the signal. The measured acceleration with the propellers on, has a maximum 2g swing which completely nullifies any attempts at attitude determination.

### TRo IMU data

Figures 5.7a, 5.7b, 5.7c, and 5.7d show plots of the accelerometer data acquired at 50Hz with the ducted fans of the TRo at zero, idle, hover, and full rotational speed, respectively. The RMS of the acceleration is listed in Table 5.2.

From Figure 5.7, the amount of noise due to the ducted fans increases proportionally to the speed of the ducted fans. The signal-to-noise ratio of the TRo is substantially larger compared to the $\mu$TRo. The high signal-to-noise ratio is due to the increased stiffness of the TRo compared to the $\mu$TRo. Figures 5.8 and 5.9 indicate an increase in Magnetometer and Gyroscope noise proportional to the rotational speed of the ducted fans.

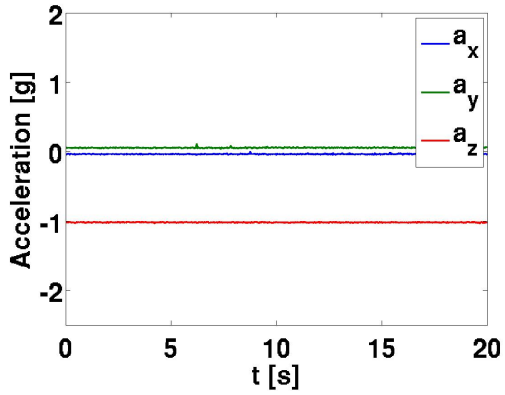


(a) Acceleration data with fans off.

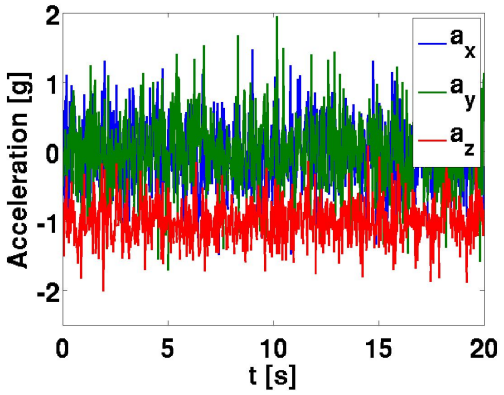


(b) Acceleration data with fans on full.

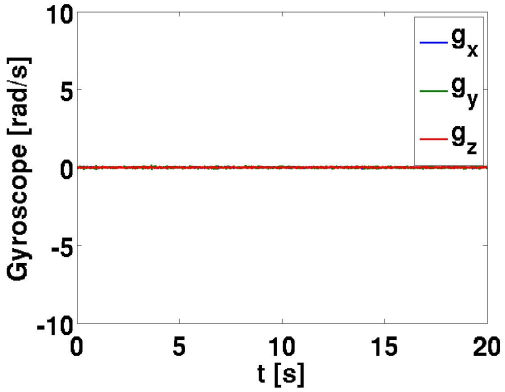


(c) Gyroscope data with fans off.

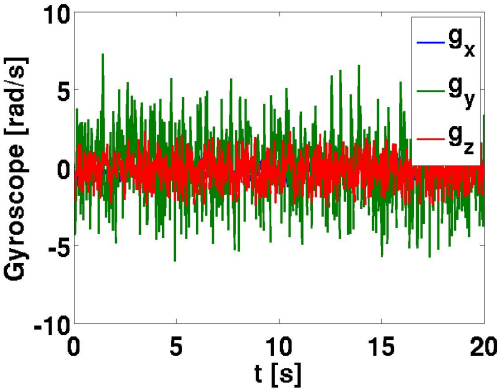


(d) Gyroscope data with fans on full.

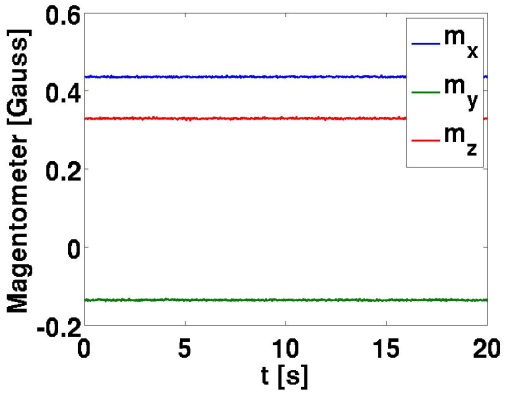


(e) Magnetometer data with fans off

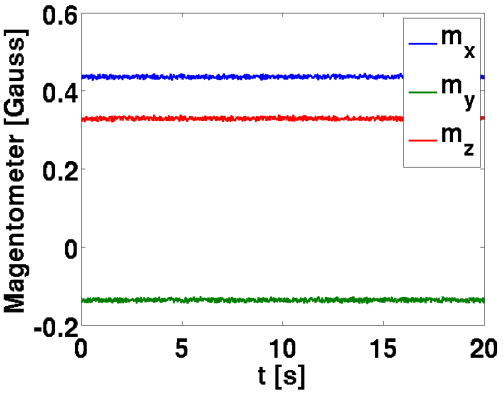


(f) Magnetometer data with fans on full.

Figure 5.6: Plots of the $\mu$TRo IMU data.

Table 5.2: The RMS of the TRo IMU measurements at multiple rotational speed of the ducted fans.

| | $a_x$ | $a_y$ | $a_z$ | $m_x$ | $m_y$ | $m_z$ | $g_x$ | $g_y$ | $g_z$ |
|---|---|---|---|---|---|---|---|---|---|
| Speed | | $[\frac{m}{s^2}]$ | | | $[Gauss]$ | | | $[\frac{rad}{s}]$ | |
| zero | 0.011 | 0.011 | 0.015 | 1.087 | 1.069 | 0.852 | 0.001 | 0.001 | 0.001 |
| idle | 0.200 | 0.184 | 0.238 | 3.694 | 3.958 | 3.005 | 0.009 | 0.010 | 0.006 |
| hover | 0.266 | 0.301 | 0.377 | 7.270 | 9.643 | 2.759 | 0.007 | 0.005 | 0.009 |
| full | 0.504 | 0.331 | 0.776 | 10.351 | 11.870 | 3.473 | 0.024 | 0.017 | 0.010 |

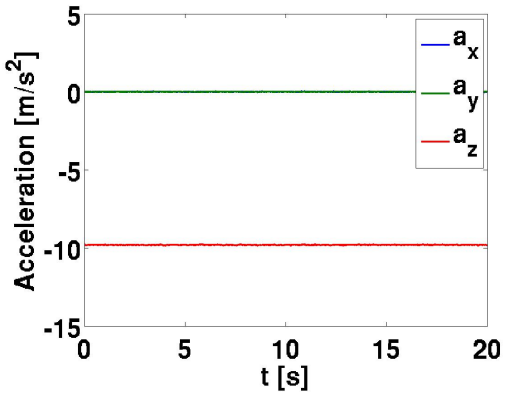


(a) Acceleration data with fans off

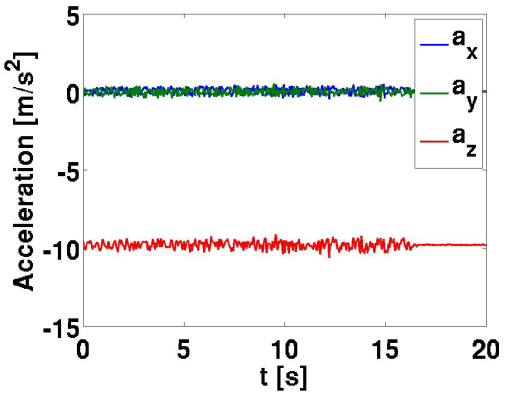


(b) Acceleration data with fans at idle

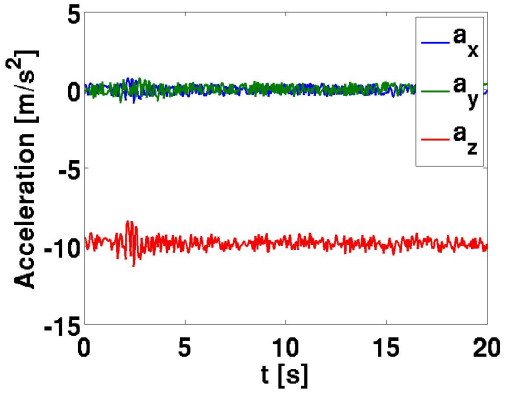


(c) Acceleration data with fans at hover

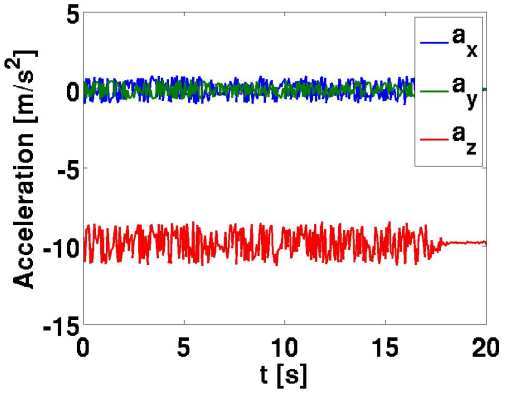


(d) Acceleration data with fans at full

Figure 5.7: Plots of the TRo acceleration data.

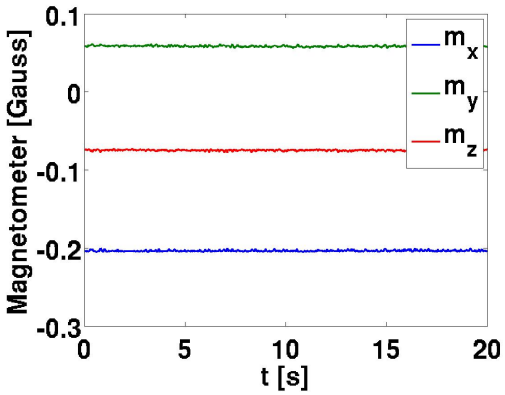


(a) Magnetometer data with fans off

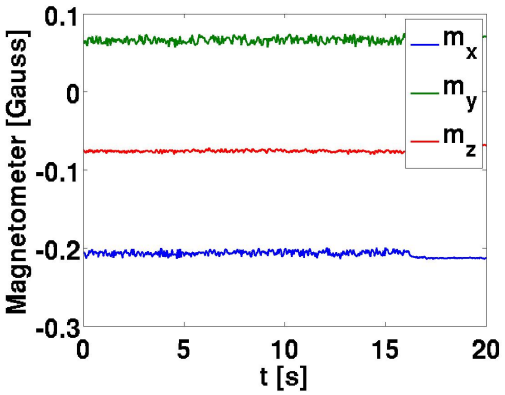


(b) Magnetometer data with fans at idle

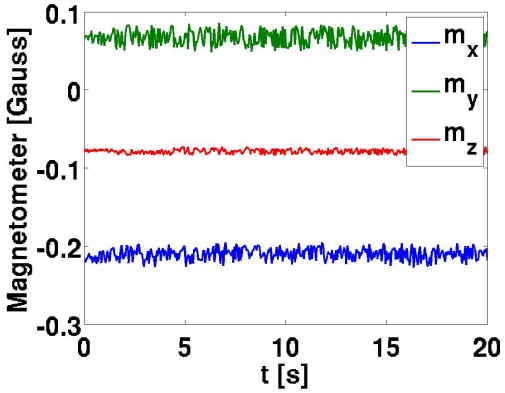


(c) Magnetometer data with fans at hover

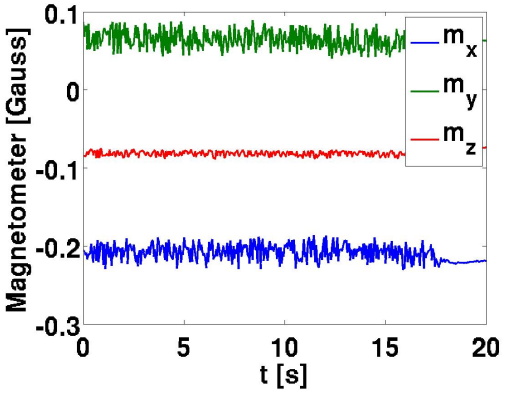


(d) Magnetometer data with fans at full

Figure 5.8: Plots of the TRo magnetometer data.

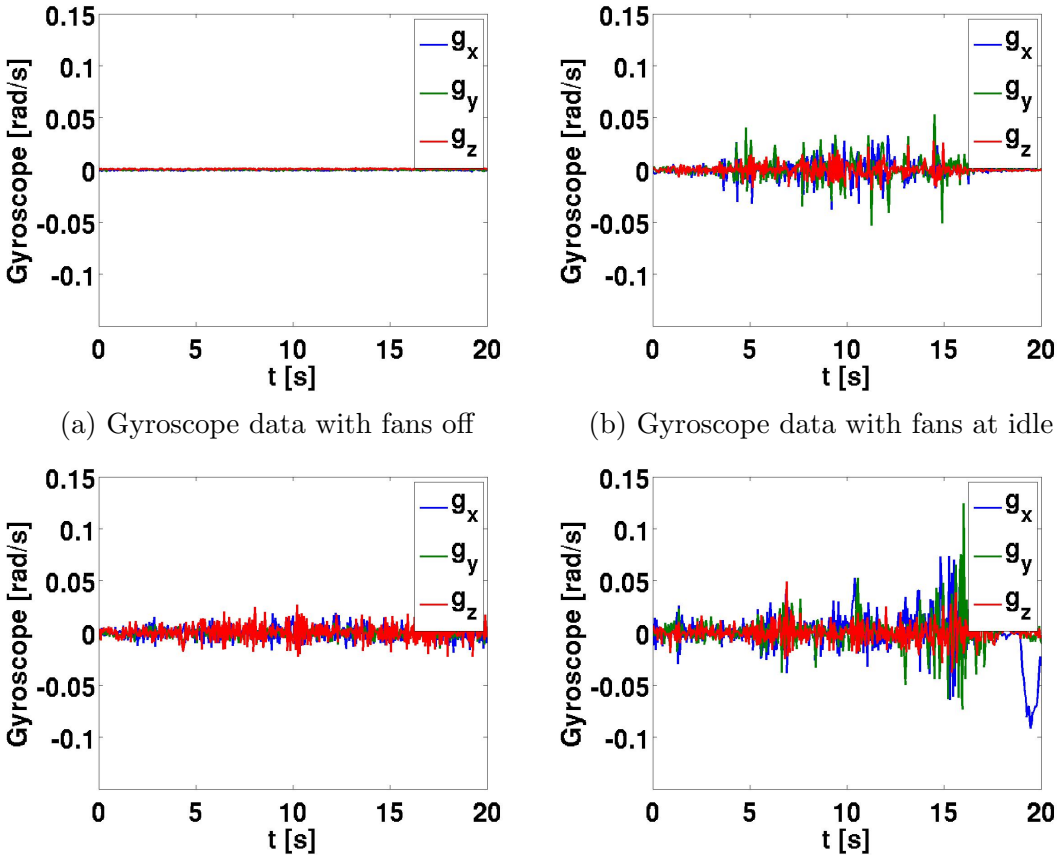


(a) Gyroscope data with fans off

(b) Gyroscope data with fans at idle

(c) Gyroscope data with fans at hover

(d) Gyroscope data with fans at full

Figure 5.9: Plots of the TRo gyroscope data.

### 5.2.3 Discussion

The completed IMU data analysis indicates that IMU noise can be rather substantial and correlates proportionally to the vibrations induced by the rotation of the propellers and ducted fans. The $\mu$TRodata shows an increased vibration along the y-axis, consistent with the frame crossbeam for both the accelerometer as well as gyroscope data suggesting that the noise is mechanical. The magnetometer data gathered from the $\mu$TRowas found to be inconclusive due to a damaged sensor. This directional noise suggests either improperly balanced propellers or inconsistent motor velocities. The noise is more significant in the $\mu$TRo and detrimental to attitude determination. Hence, the current configuration and design of the $\mu$TRo is inadequate for autonomous flight using on-board sensors. It is possible to utilize an external 3D pose tracking system with a high update rate to provide orientation feedback of the system for controlled motion. The RMS for the acceleration measurements with the TRo running at full speed is $0.776\frac{m}{s^2}$.

## 5.3 Remotely Controlled Altitude and Yaw

An experimental demonstration of the $\mu$TRo and TRo hovering with remotely controlled altitude and heading was completed while the systems were tethered. Figures 5.10 and 5.11 show a snapshot of both prototypes hovering. The $\mu$TRo was constrained using fishing line. The fishing line was passed through two circular openings vertically aligned along the main structure. The constraint prevented the $\mu$TRo from pitching or rolling and allowed the system to yaw and translate vertically. More significant considerations were used when testing the TRo. The TRo was constrained using a steel rod and linear bearings. As with the $\mu$TRo, the TRo was constrained against pitching and rolling but allowed yaw rotation and vertical translation.

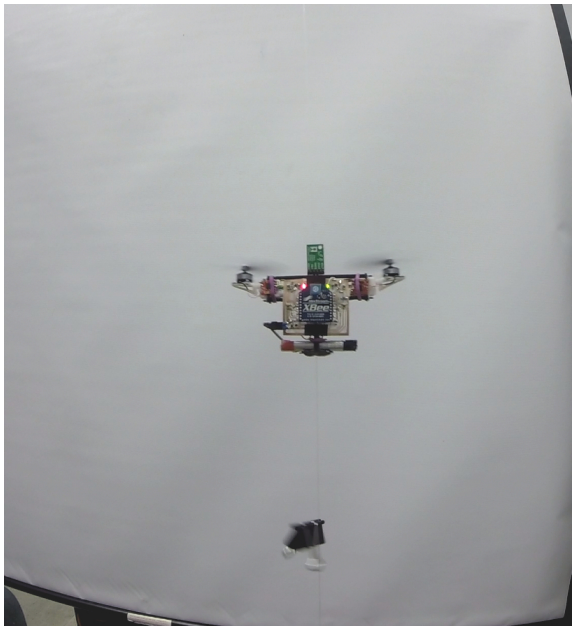

Figure 5.10: $\mu$TRo hovering with remotely controlled altitude and yaw control.

For both prototypes, the on-board controller ran the developed control algorithm. The feedback error was directly replaced with reference signal provided by the human controller over wireless communication. The altitude command reference was scaled and the control signal was saturated to a maximum value of 1200 microseconds, above the hover control output value. For the $\mu$TRo, a computer program was created to read USB joystick information and send the joystick reference command to the $\mu$TRo at 50Hz. For the TRo, a RC transmitter and receiver were used. The RC receiver output was connected to the APM RC inputs. The RC inputs were read at each controller update cycle and used as the reference command.

## 5.4 Summary

This chapter measured the performance of the propellers and ducted fans, analyzed the IMU data, and presented the experimental demonstration of the tiltrotor pro-


Figure 5.11: TRo hovering with remotely controlled altitude and yaw control.

totypes in hover with remotely controlled altitude and yaw control.

# Chapter 6

# Discussion and Future Work

## 6.1 Discussion

The following sections discuss the project successes, difficulties, and limitations in the modeling and production of a realized tiltrotor system. Discussed in detail, is the component selection, manufacturing processes and techniques, control algorithms, design trade-offs, and system scalability. Avenues for future work are suggested including, the recommendation of future flight testing, suggestions towards the use of control strategies for aggressive maneuvers, vibration analysis and reduction, and finally recommendations specific to future design iterations.

### 6.1.1 Component Selection

The micro scale tiltrotor platform is designed to be a complete robotic solution intended for indoor proof of concept testing that is cost effective, power efficient, and fully autonomous. The realization of this system is further constrained by the desire to produce the vehicle on the micro scale. The full scale tiltrotor, however, is designed to operate both indoors and outdoors, again fully autonomously, but

capable of aggressive flight maneuvers and overall high performance. As such many difficulties were encountered during the realization of either system. As is true with the design of any system, the process is both cyclical and iterative. For this project the driving forces for both systems were flight duration and overall thrust power. Component selection for both the micro and full scale robot were limited to parts sourced from hobby supply outlets. Although diverse in the range of components offered, often the desired components, were either difficult to source within the allotted time frame, were presented as having significantly higher performance than testing and implementation would suggest, or were simply unavailable for purchase.

The major trade-off with regards to the dual-nacelle tiltrotor aerial vehicle is the duration of flight versus weight and payload capacity. This constraint drove the motor selection for both robots, requiring careful consideration of thrust to weight ratio and mounting constraints. Without sufficient information documenting motor and propeller performance for the micro scale system, empirical based testing was conducted on multiple motor and propeller combinations. This testing was used to converge on a solution that produced the highest sum of thrust to power and thrust to weight ratio for the desired voltage. The full scale tiltrotor platform design utilized ducted fans units for the following reasons: they maintain high thrust output at high motor speeds, have low propeller inertia due to their shortened airfoil length and thickness, have a higher efficiency than similar sized proprotors, and include an inherent safety mechanism due to the propeller housing. The decision to utilize ducted fan units restricted the number of available solutions for the full size system. At the time of this system design and development, very few high static thrust ducted fans were available, with even fewer options available for counter rotational propellers, despite being the obvious choice for this application.

The design goals outlined a 15 minute flight duration, but with limited space

and weight for carrying a battery, it was soon determined unobtainable. Increasing the flight duration generally requires larger batteries which in turn increases weight and necessary structural support. Batteries are available in a wide range of configurations, weights, and power densities, among the most readily available and power dense are the Lithium Polymer (LiPo) batteries. These batteries are very common among hobby aircraft and ground vehicles for their fast charge, and discharge rates, as well as their compact size. The battery voltage is defined by the number of cells contained within the pack. Consequently most hobby components are designed with these voltages in mind and as such they were the most obvious choice for both platforms.

For this project two different embedded microcontrollers were used. In the first prototype an off the shelf autopilot was chosen to reduce the amount of redundant embedded software that was to be written and to increase the speed of the project realization. The controller was available with open source libraries for interfacing with the multitude of components offered both on-board and as plug in solutions. The second microcontroller used was the Atmega 88p. It was determined during the initial test phases that this microcontroller was a substantial limiting factor to prototype functionality. The processor offered a maximum of 8KB of flash memory, of which the initial implementation of the on board attitude controller, PPM signal generator, and $I^2C$ command bus alone exceeded 6KB. The on board 8Mhz oscillator was determined to be performance limiting for sensor data acquisition, control algorithm processing, and control variable outputs. A temporary solution was to bypass the embedded 8Mhz oscillator with the use of an external 20Mhz oscillator, the maximum rated option, allowing for faster processing.

Communication between the platform and an external computer provided yet another challenge for both the micro and full scale robot. Wireless telemetry

was prone to delays, unevenly prioritized bidirectional communication, and lost or corrupt signals packets

## 6.2 Future Work

With the success of both prototypes demonstrated in tethered hover mode and the development of a MATLAB® Simulink block for simulation and control verification, multiple future areas of research may be explored. The following sections describe possible continued work on the dual-nacelle tiltrotor aerial vehicle.

### 6.2.1 Flight Testing

Our preliminary work on the full system testing in Chapter 2 has proven the concept aerial vehicle controllable even when computationally under powered. Further work, in testing both the $\mu$TRo and TRo realized systems, has shown that both systems are viable for flight in the real world with the addition of more accurate system attitude measurements. It is recommended that further analysis be completed on both the constrained flight of the system and further increasing the active state space of the system to the full 6 DoF with the use of a safety line to prevent crashes.

### 6.2.2 Control Strategies for Aggressive Maneuvers

Although the dual-nacelle tiltrotor prototypes are capable of more aggressive maneuvers, the presented PD control strategy is rather limited. Currently the system is capable of stable hover and four dimensional pose-to-pose with yaw rotation, control of the aerial vehicle. A controller capable of aggressive maneuvers is desirable especially when attempting to quickly navigate cluttered and close-quarter environments. Future work would be based in the discovery of state space trajectory

controllers with varying optimization functions that consider the dynamics and energy of the system while attempting to minimize maneuver time. These controllers could be implemented using discreet methods including A*, D* or Rapid-Exploring Random Trees (RRT). More challenging would be the implementation of the search algorithms on a resource constrained system such as the micro scale dual-nacelle tiltrotor prototype.

### 6.2.3 Vibration Analysis and Damping $\mu$TRo

The micro scale dual-nacelle tiltrotor experienced sever acceleration noise due propeller noise during operation. This noise greatly affected the attitude and heading reference system. Future research on the system would include a numerical 3D modal-analysis of the current design with validation through structural vibration experiments. The vibrations could be caused by a few factors including vortex shedding from the propellers, improper balancing of the propeller blades, imbalanced installation of the propellers, uneven motor speeds, and general oscillations of the propellers passing through the natural frequency of the structure. The results of the modal analysis would then be used to optimize the design for a light weight, stiffer structure. Additional damping methods could be implemented including the installation of rubber internal to the structural tubing or damping isolation of the IMU. The use of composite materials could also be studied and their affect on the structural vibrational modes could be analyzed. Additional work could focus on of inclusion of low pass filters to supplement the mechanical damping. These filters would remove some of the more aggressive sensor measurements from the data sampling, allowing for a smoother approximation of the current system state within the self contained autonomous controller.

### 6.2.4 Redesign of the Full Scale Dual-Nacelle Tiltrotor

The current design of the full scale dual-nacelle tiltrotor was based on the availability of the 3D printer which lead to a light weight but structurally weak design. Flight testing completed with the current design resulted in structural failures due to large centripetal accelerations and high velocity landings. Future work focused on the redesign of the full scale dual-nacelle tiltrotor would include thrust bearings on the shafts connecting the nacelles and the use stronger materials such as metal or carbon fiber.

# Chapter 7

# Conclusions

This thesis has presented the study on the feasibility of the control and realization of a dual-nacelle tiltrotor aerial vehicle designed for aggressive flight maneuvering within cluttered and restrictive environments. A multi-body dynamic model of a dual-nacelle tiltrotor aerial vehicle was derived based on the Newton-Euler method. A simplified dynamic model of a dual-nacelle tiltrotor was also derived for the aerial vehicle utilizing a single body approach to simplify the control implementation. A MATLAB® Simulink block was implemented based on the full dynamic model of the tiltrotor. The Simulink block was used to simulate the dual-nacelle tiltrotor, verify control strategies, and tune control parameters.

A non-linear PD attitude and altitude controller was designed for the dual-nacelle tiltrotor based on the simplified derived dynamic model. The non-linear PD controller was verified in simulation using the implemented MATLAB® Simulink block. The implemented MATLAB® Simulink block was augmented to include a realistic model of the tilting servo by considering the control dynamics of the internal servo controller and a model of the system response delay due to the PWM output frequency of 50Hz by using a zero order hold. The simulation was used to tune

the controller parameters based on the system dynamics and physical properties. The controller was verified able to do point-to-point relocation and track a spacial trajectories.

Two dual-nacelle tiltrotor prototypes were designed and realized. The prototypes consisted of a 0.5m wide, 2.8kg tiltrotor and a 50mm wide, 30g tiltrotor. An in-depth description of the realization process is provided including component selection, structural design, body manufacturing, and software implementation methods. The experimental setup and data analysis of prototype components was presented. The hovering capability of both tiltrotor prototypes was demonstrated through tethered operation. Discussion on the design and scalability considerations for dual-nacelle tiltrotor aerial vehicles was addressed. Empirical data on the efficiency of individual components for a tiltrotor aerial vehicle were presented and discussed. Future work for the development of scaled tiltrotor designs is suggested. The dual-nacelle tiltrotor prototypes presented herein provide a platform for future research on the control strategies for aggressive maneuvers of underactuated aerial vehicles.

# Bibliography


[1] D. J. Pines and F. Bohorquez, "Challenges facing future micro-air-vehicle development," *Journal of Aircraft*, vol. 43, no. 2, pp. 290–305, 2006.

[2] J. Lin, H. Tao, Y. Wang, and Z. Huang, "Practical application of unmanned aerial vehicles for mountain hazards survey," in *Proceedings of the International Conference on Geoinformatics*, pp. 1–5, June 2010.

[3] T. Samad, J. Bay, and D. Godbole, "Network-Centric Systems for Military Operations in Urban Terrain: The Role of UAVs," *Proceedings of the IEEE*, vol. 95, no. 1, pp. 92–107, 2007.

[4] T. Tomic, K. Schmid, P. Lutz, A. Domel, M. Kassecker, E. Mair, I. Grixa, F. Ruess, M. Suppa, and D. Burschka, "Toward a Fully Autonomous UAV: Research Platform for Indoor and Outdoor Urban Search and Rescue," *IEEE Robotics Automation Magazine*, vol. 19, no. 3, pp. 46–56, 2012.

[5] S. Waharte and N. Trigoni, "Supporting Search and Rescue Operations with UAVs," in *Proceedings of the International Conference on Emerging Security Technologies (EST)*, pp. 142–147, Sept 2010.

[6] M. Montenegro Campos and L. de Souza Coelho, "Autonomous dirigible navigation using visual tracking and pose estimation," in *Proceedings of the IEEE International Conference on Robotics and Automation (ICRA)*, vol. 4, pp. 2584–2589 vol.4, 1999.

[7] N. Sharkey, "Death strikes from the sky: the calculus of proportionality," *IEEE Technology and Society Magazine*, vol. 28, pp. 16–19, Spring 2009.

[8] N. Michael, D. Mellinger, Q. Lindsey, and V. Kumar, "The GRASP Multiple Micro-UAV Testbed," *IEEE Robotics Automation Magazine*, vol. 17, pp. 56–65, Sept 2010.

[9] G. Cai, B. Chen, K. Peng, M. Dong, and T. Lee, "Modeling and Control of the Yaw Channel of a UAV Helicopter," *IEEE Transactions on Industrial Electronics*, vol. 55, pp. 3426–3434, Sept 2008.

[10] S. McIntosh, S. Agrawal, and Z. Khan, "Design of a mechanism for biaxial rotation of a wing for a hovering vehicle," *IEEE/ASME Transactions on Mechatronics*, vol. 11, pp. 145–153, April 2006.

[11] W. Green and P. Oh, "Autonomous hovering of a fixed-wing micro air vehicle," in *Proceedings of the International Conference on Robotics and Automation (ICRA)*, pp. 2164–2169, May 2006.

[12] A. J. Barry, "Flying Between Obstacles with an Autonomous Knife-Edge Maneuver," Master's thesis, Massachusetts Institute of Technology, Sep 2012.

[13] K. Ma, S. Felton, and R. Wood, "Design, fabrication, and modeling of the split actuator microrobotic bee," in *Proceedings of the IEEE/RSJ International Conference on Intelligent Robots and Systems (IROS)*, pp. 1133–1140, Oct 2012.

[14] "Aerovironment Hummingbird," April 2014.

[15] S. Salazar-Cruz and R. Lozano, "Stabilization and nonlinear control for a novel trirotor mini-aircraft," in *Proceedings of the IEEE International Conference on Robotics and Automation (ICRA)*, pp. 2612–2617, 2005.

[16] A. Briod, P. Kornatowski, J.-C. Zufferey, and D. Floreano, "A Collision-resilient Flying Robot," *Journal of Field Robotics*, 2013.

[17] F. Senkul and E. Altug, "Modeling and control of a novel tilt Roll rotor quadrotor UAV," in *Proceedings of the International Conference on Unmanned Aircraft Systems (ICUAS)*, pp. 1071–1076, May 2013.

[18] M. Ryll, H. Bulthoff, and P. Giordano, "First flight tests for a quadrotor UAV with tilting propellers," in *Proceedings of the International Conference on Robotics and Automation (ICRA)*, pp. 295–302, May 2013.

[19] A. Sanchez, J. Escareo-Castro, O. Garcia-Salazar, and R. Lozano, "Autonomous Hovering of a Noncyclic Tiltrotor UAV: Modeling, Control and Implementation," in *Proceedings of the World Congress on International Federation of Automatic Control (IFAC)*, pp. 803–808, July 2008.

[20] S. S. Dhaliwal and A. Ramirez-Serrano, "Control of an unconventional VTOL UAV for search and rescue operations within confined spaces based on the MARC control architecture," in *Proceedings of the IEEE International Workshop on Safety, Security Rescue Robotics (SSRR)*, pp. 1–6, Nov 2009.

[21] C. Papachristos, K. Alexis, G. Nikolakopoulos, and A. Tzes, "Model predictive attitude control of an unmanned Tilt-Rotor aircraft," in *Proceedings of the IEEE International Symposium on Industrial Electronics (ISIE)*, pp. 922–927, June 2011.

[22] F. Goncalves, J. Bodanese, R. Donadel, G. Raffo, J. Normey-Rico, and L. Becker, "Small scale UAV with birotor configuration," in *Proceedings of the International Conference on Unmanned Aircraft Systems (ICUAS)*, pp. 761–768, May 2013.

[23] O. Kreisher, "Finally, the Osprey," *Air Force Magazine*, February 2009.

[24] J. J. Craig, *Introduction to Robotics: Mechanics and Control*. Prentice Hall, 2004.

[25] S. Madgwick, A. J. L. Harrison, and R. Vaidyanathan, "Estimation of IMU and MARG orientation using a gradient descent algorithm," in *Proceedings of the IEEE International Conference on Rehabilitation Robotics (ICORR)*, pp. 1–7, June 2011.

[26] R. Mahony, T. Hamel, and J.-M. Pflimlin, "Nonlinear Complementary Filters on the Special Orthogonal Group," *IEEE Transactions on Automatic Control*, vol. 53, pp. 1203–1218, June 2008.

[27] I. Palunko, P. Cruz, and R. Fierro, "Agile Load Transportation: Safe and Efficient Load Manipulation with Aerial Robots," *IEEE Robotics Automation Magazine*, vol. 19, pp. 69–79, Sept 2012.

[28] A. Ollero and L. Merino, "Control and perception techniques for aerial robotics," *Annual Reviews in Control*, vol. 28, no. 2, pp. 167–178, 2004.

[29] J. A. Vilchis, B. Brogliato, A. Dzul, and R. Lozano, "Nonlinear modelling and control of helicopters," *Automatica*, vol. 39, no. 9, pp. 1583–1596, 2003.

[30] S. Lee, C. Ha, and B. Kim, "Adaptive nonlinear control system design for helicopter robust command augmentation," *Aerospace Science and Technology*, vol. 9, no. 3, pp. 241–251, 2005.

[31] P. Oh, M. Joyce, and J. Gallagher, "Designing an aerial robot for hover-and-stare surveillance," in *Proceedings of the International Conference on Advanced Robotics (ICAR)*, pp. 303–308, 2005.

[32] W. Kang, B. Chen, K. Peng, M. Dong, and T. Lee, "Modeling and Control System Design for a UAV Helicopter," in *Proceedings of the Mediterranean Conference on Control and Automation (MED)*, pp. 1–6, 2006.

[33] B. Mettler, M. B. Tischler, and T. Kanade, "System identification modeling of a small-scale unmanned rotorcraft for flight control design," *Journal of the American Helicopter Society*, vol. 47, no. 1, pp. 50–63, 2002.

[34] J.-G. Juang and W.-K. Liu, "Hardware Implementation of a Hybrid Intelligent Controller for a Twin Rotor MIMO," in *Proceedings of the International Conference on Innovative Computing Information and Control (ICICIC)*, pp. 185–185, 2008.

[35] W. Kang, K. Peng, B. Chen, and T. Lee, "Design and assembling of a UAV helicopter system," in *Proceedings of the International Conference on Control and Automation (ICCA)*, vol. 2, pp. 697–702, 2005.

[36] S. Bouabdallah, R. Siegwart, and G. Caprari, "Design and Control of an Indoor Coaxial Helicopter," in *Proceedings of the IEEE/RSJ International Conference on Intelligent Robots and Systems (IROS)*, pp. 2930–2935, 2006.

[37] S. Sato, *Design and characterization of Hover Nano Aerial Vehicle (HNAV) propulsion system*. PhD thesis, Massachusetts Institute of Technology, 2008.

[38] F. Bohorque, P. Samuel, J. Sirohi, D. Pines, L. Rudd, and R. Perel, "Design, Analysis and However Performance of a Rotary Wing Micro Air Vehicle," *Journal of the American Helicopter Society*, vol. 48, no. 2, pp. 80–90, 2003.

[39] G. B. Kim, I. H. Paik, K. J. Yoon, H. C. Park, and N. S. Goo, "Manufacturing and Performance Test of Rotary Wing-type Micro Aerial Vehicle," in *Proceedings of the AIAA "Unmanned Unlimited" Technical Conference, Workshop and Exhibit*, pp. 1–5, 2004.

[40] S. D. Prior, M. Karamanoglu, S. Odedra, T. Foran, and M. A. Erbil, "Development of a co-axial tri-rotor UAV," in *Proceedings of International Unmanned Aerial Vehicle Systems Conference*, 2009.

[41] D.-W. Yoo, H.-D. Oh, D.-Y. Won, and M.-J. Tahk, "Dynamic modeling and control system design for Tri-Rotor UAV," in *Proceedings of the International Symposium on Systems and Control in Aeronautics and Astronautics (ISSCAA)*, pp. 762–767, 2010.

[42] S. Gupte, P. Mohandas, and J. Conrad, "A survey of quadrotor Unmanned Aerial Vehicles," in *Proceedings of IEEE Southeastcon*, pp. 1–6, 2012.

[43] D. Lara, G. Romero, A. Sanchez, R. Lozano, and A. Guerrero, "Robustness margin for attitude control of a four rotor mini-rotorcraft: Case of study," *Mechatronics*, vol. 20, no. 1, pp. 143–152, 2010.

[44] C. Bills, J. Chen, and A. Saxena, "Autonomous MAV flight in indoor environments using single image perspective cues," in *Proceedings of the IEEE International Conference on Robotics and Automation (ICRA)*, pp. 5776–5783, 2011.

[45] A. Bachrach, A. Garamifard, D. Gurdan, R. He, S. Prentice, J. Stumpf, and N. Roy, "Co-ordinated tracking and planning using air and ground vehicles," in *Proceedings of the International Symposium on Experimental Robotics*, pp. 137–146, 2009.

[46] J. Dietsch, "Air and Sea Robots Add New Perspectives to the Global Knowledge Base [News and Views]," *IEEE Robotics & Automation Magazine*, vol. 18, no. 2, pp. 8–9, 2011.

[47] M. Maurer, M. Rumpler, A. Wendel, C. Hoppe, A. Irschara, and H. Bischof, "Geo-referenced 3D reconstruction: Fusing public geographic data and aerial imagery," in *Proceedings of the International Conference on Robotics and Automation (ICRA)*, pp. 3557–3558, 2012.

[48] S. Yanguo and W. Huanjin, "Design of Flight Control System for a Small Unmanned Tilt Rotor Aircraft," *Chinese Journal of Aeronautics*, vol. 22, no. 3, pp. 250–256, 2009.

[49] J. H. Ginsberg, *Advanced Engineering Dynamics*. Cambridge University Press, 1998.